Trimetallic oxide-hydroxide porous nanosheets for efficient water oxidation

Hemam Rachna Devi[a,c], *Ramachandra Chikkegowda*[b], *Dinesh Rangappa*[b], *Ashok Kumar Yadav*[c], *Zhong Chen**[d], *Karuna Kar Nanda**[a]

E-mail: nanda@iisc.ac.in

a. Materials Research Centre, Indian Institute of Science, Bangalore 560012, India.

b. Visvesvaraya Technological University, Bangalore, India.

c. Atomic and Molecular Physics Division, Bhabha Atomic Research Centre, Trombay, Mumbai-400085, India.

d. School of Materials Science and Engineering, Nanyang Technological University, 50 Nanyang Avenue, Singapore 639798, Singapore

Keywords: Trimetallic oxide-hydroxide, water oxidation, electrocatalyst, intrinsic activity, flat-band potential.

Abstract

Multimetallic systems have been the subject of intensive research for their promising electrocatalytic activities. Herein, we describe the synthesis of bimetallic and trimetallic (Ni, Co and Mn) oxide-hydroxide nanosheets and evaluate their catalytic activity toward water oxidation. The catalytic activity of porous trimetallic nanosheets was found to be higher than that of bimetallic hybrids. In addition, the trimetallic systems also possess excellent stability. A current density of 10 mA/cm^2 is achieved for an overpotential of 287 mV and ~0% loss even after 8000 cycles. The enhanced performance by the trimetallic system can be attributed to the large electrochemical surface area and better intrinsic activity. The electronic modulation in this three-element system is evident from the X-Ray Photoelectron Spectroscopy (XPS) study and Mott-Schottky analysis. The position of flat-band potential plays a significant role in determining the charge transfer kinetics, thereby affecting the water oxidation activity in the semiconductor-electrolyte system. Trimetallic system also offers better oxygen evolution reaction kinetics as evident from the least activation energy compared to the bimetallic counterparts. The local structure system is realized with the X-ray absorption spectroscopy (XAS) analysis. The present study highlights the importance of intrinsic activity in designing efficient non-noble metal electrocatalysts.

1. Introduction

The search for sustainable energy sources has resulted in immense attention towards the production and storage of hydrogen - a neat and clean fuel that can be an alternative to petroleum-based energy sources. Consumption of fossil fuels has caused severe environmental problems due to the release of toxic byproducts.[1] In this aspect, water splitting is a clean and renewable

alternative,[2] though the process is hindered by sluggish oxygen kinetics in water oxidation reaction/oxygen evolution reaction (OER).[3,4] Efforts are being made to develop catalysts that are cost-effective, efficient and durable for OER. In this regard, various materials have been explored as an efficient electrocatalysts, including transition metal oxides, sulfides, phosphides, etc.[5–13] Transition metal-based oxides or hydroxides are potential alternatives due to their rich redox property and excellent stability in an oxidizing environment. [14] Until now, a wide range of first-row transition metal-based oxides/hydroxides/oxyhydroxides have been investigated for water oxidation.[15,16,25,26,17–24][27] The electrocatalytic activity of the monometallic system is limited by its poor electronic conductivity. Bimetallic systems have shown better conductivity over monometallic systems due to the hybridization of the constituent elements.[28,29] Ni-Fe-based binary oxide/(oxy) hydroxide seems to be the best performing OER catalyst till date.[30–35] Incorporation of a third element into a bimetallic system modulates the electronic structure thereby impacting on adsorption energy of the reaction intermediates (thermodynamics) and conductivity (kinetics) for the water oxidation.[36,37] Though the former has been extensively studied,[38–40] the basic understanding of the mechanism for better kinetics in semiconductor electrocatalyst like oxide/hydroxide is lacking in the literature.

Trimetallic oxide/(oxy)hydroxides based on first-row transition metal have been considered to be a new class of water oxidation electrocatalysts. [41,42,51–53,43–50] They were also reported to exhibit superior activity over bimetallic and monometallic systems.[37,47,54–60] Further, the hybrid oxide-hydroxide structure has shown superior water oxidation performance over their pristine oxide or hydroxide.[61] Moreover, a 2-dimensional (2D) nanosheet with porous structures can provide more active sites for electrocatalytic reactions[26,62] and providing easy access of the

electrolyte to the active sites.[63] Synergistic electronic and morphological modulation is, therefore, an effective route to design an efficient catalyst for OER.[64]

Herein, we have synthesized trimetallic cobalt, nickel, and manganese oxide-hydroxide hybrid porous nanosheets via a simple and cost-effective hydrothermal method. Nickel-cobalt oxide - hydroxide were explored as efficient oxygen evolution catalyst.[65] The incorporation of high valence state elements promotes catalytic activity.[66,67] According to the Sabatier principle, the binding of the reaction intermediates should be optimum for efficient reaction. The descriptor for prediction of optimum adsorption of reaction intermediate is the volcano plot (adsorption-energy scaling relationships). RuO_2 and IrO_2 known to possess best OER activity are located around the top of the volcano plot. [68,69] After Co and Ni, Mn based oxide lies close to the peak of the volcano plot.[70] In this regard, Mn is a good choice as the third element for our system.

The local structure of the trimetallic (Co/Ni/Mn) based system is investigated by X-ray Near-Edge Structure (XANES) and Extended X-ray Absorption Fine Structure (EXAFS) techniques.[71] The as-synthesized trimetallic system exhibits, lower onset potentials (247 mV at current density of 2 mA/cm^2 and 287 mV at current density of 10 mA/cm^2), and a lower Tafel slope of 53 mV/dec when compared with the corresponding bimetallic systems. It also exhibits good operational stability (8000 cycles) and durability (20h). Moreover, we have elucidated the role of flat-band potential, activation energy and highlight the importance of intrinsic activity in water oxidation kinetics. The reaction intermediate was probed by methanol oxidation reaction and the adsorption energy was deduced. In the current work, the flat-band potential was determined by the Mott-Schottky analysis.[72–74] The dependency of various parameters like

charge transfer resistance, Tafel slope, onset and overpotential on the flat-band potential has been studied. The maximum flat-band potential corresponded to a minimal charge transfer resistance in the trimetallic system. This serves as evidence for the electronic modulation that has resulted in its superior kinetics over the bimetallic counterparts. The present study elucidates the semiconductor-electrolyte interface behavior along with the reaction kinetics through an improved understanding of the enhanced water oxidation of the trimetallic oxide-hydroxide nanosheet catalysts.

2. Experimental section

Synthetic procedures. For the synthesis of trimetallic cobalt nickel manganese oxide-hydroxide hybrid (CNM), an appropriate amount of cobalt nitrate hexahydrate, nickel nitrate hexahydrate and manganese acetate tetrahydrate has been mixed in the molar ratio 1:1:1 (7 mM) with 0.02 M hexamethylenetetramine (HMT) and stirred for 30 minutes. The homogeneous solution has been fed into a 100 ml Teflon-lined autoclave which was heated at 70 ^{o}C for 24 h. For the synthesis of the bimetallic system (NM: nickel-manganese oxide-hydroxide, CM: cobalt-manganese oxide-hydroxide, CN: cobalt-nickel oxide-hydroxide), respective salts are mixed in the molar ratio 1:1 (10.5 mM) with the same amount of HMT and followed the same procedure as that for CNM. The obtained precipitates were collected and annealed at 300 °C for 1 h at the ramping rate of 5 °C per min.

Characterizations. X-ray diffraction (XRD) studies were carried out using PANalytical with Cu Kα as the source. The ULTRA 55 Field Emission Scanning Electron Microscope and High-Resolution Transmission Electron Microscopy (HRTEM) were used for morphological characterization. High-angle annular dark-field scanning transmission electron microscopy (HAADF-STEM) and elemental mapping were obtained by TEM-TITAN Themis at 300 kV. For obtaining Raman spectra have been acquired using WITEC spectrophotometer with 532 nm

excitation. X-ray photoelectron spectroscopy (XPS) studies were carried out using AXIS ULTRA for compositional analysis. Inductively Coupled Plasma Mass Spectrometer (ICPMS, Thermo X Series II) was used for the determination of the elemental concentrations. Quantachrome Instrument was used for Brunauer–Emmett–Teller (BET) surface area measurements.

XAS measurements, comprising of both XANES and EXAFS techniques, were carried out at room temperature in transmission mode using the Energy-Scanning EXAFS beamline (BL-9) at the Indus-2 Synchrotron Source (2.5 GeV, 100 mA). [75][76]

Electrochemical measurements. All the electrochemical measurements were carried out using a CHI electrochemical workstation which consists of an electrochemical cell with a three-electrode system. The electrodes comprise of Ag/AgCl as the reference, Pt-C as the counter and catalyst-modified glassy carbon as the working electrode. All the measurements were carried out in 1M NaOH (pH=13.6) solution [62]. For catalyst preparation, 7 mg of the electrocatalyst were dispersed in 1 ml of ethanol and water as a solvent mixed in equal proportion and ultrasonicated for 30 min to obtain a slurry. 15 μl of Nafion (binder) is added into 100 μl of the as as-obtained slurry and further sonicated for 15 min. An appropriate amount of catalyst slurry is loaded on a glassy carbon electrode for further electrochemical measurements. For the poison study, 10 mM sodium cyanide (NaCN) was added in 1M NaOH solution. The Mott-Schottky measurements were carried out in 1 M NaOH solution at a scan rate of 10 mV/s at 100 Hz. The electrochemical impedance spectroscopy was measured in 1 M NaOH solution at 1.423 V vs RHE. For methanol oxidation reaction, electrocatalyst was drop casted on rotating ring disc electrode (RRDE) and LSV measurement was carried out N_2 saturated 1 M NaOH electrolyte in absence and presence of 1 M methanol and the Pt-ring was set at a potential of 0.25 V vs RHE.

3. Results and discussion

Trimetallic Co-Ni-Mn-based oxide-hydroxide porous nanosheets have been synthesized using hydrothermal synthesis and were denoted as CNM. Bimetallic oxides-hydroxide nanosheets of cobalt-nickel, nickel-manganese and cobalt-manganese were synthesized under identical conditions and were named CN, NM and CM, respectively. The schematic of the synthesis of porous nanosheets is presented in Figure 1. XRD studies were carried out for crystal structural identification of CNM samples before (CNMBA) and after (CNM) annealing. As shown in Figure S1a for CNM, peaks around 11.39°, 18.93° and 22.70° represent the (003), (001) and (006) crystalline planes of cobalt-nickel-manganese hydroxide [ICDD-04-018-1384][28,57], 37.67°, 43.69° and 63.67° represents the (222), (400) and (440) facet of corresponding trimetallic oxide [ICDD-04-019-8823]. Figure S1b shows the Raman spectra where a broad peak was observed around 500 cm $^{-1}$, which signifies the presence of an M-O-M bond (M: Co/Ni/Mn).[77,78] These results confirm that $M(OH)_2$ nanosheets (M: Co, Ni, Mn) along with the intermediates were obtained after the hydrothermal treatment. The thermal decomposition of these intermediates during annealing leads to the release of NH_3, ONO^-, NO_3^- and CO_2 leaving behind porous trimetallic oxide-hydroxide nanosheets[79,80].

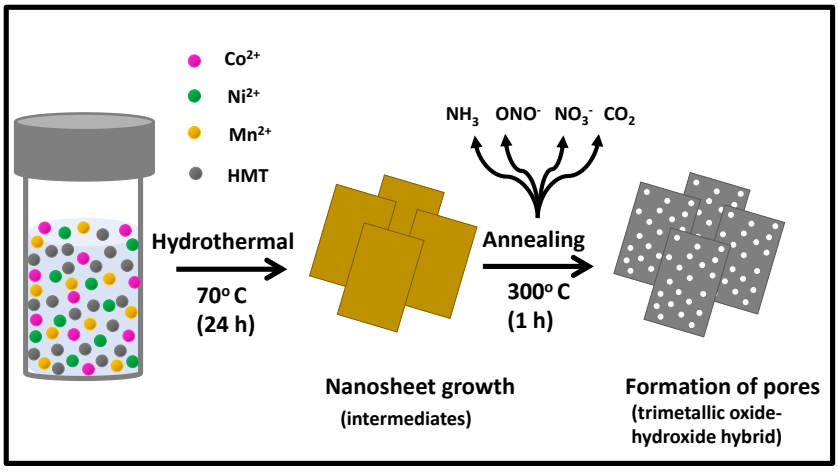

Figure 1. Schematic of the synthesis of porous trimetallic oxide-hydroxide hybrid.

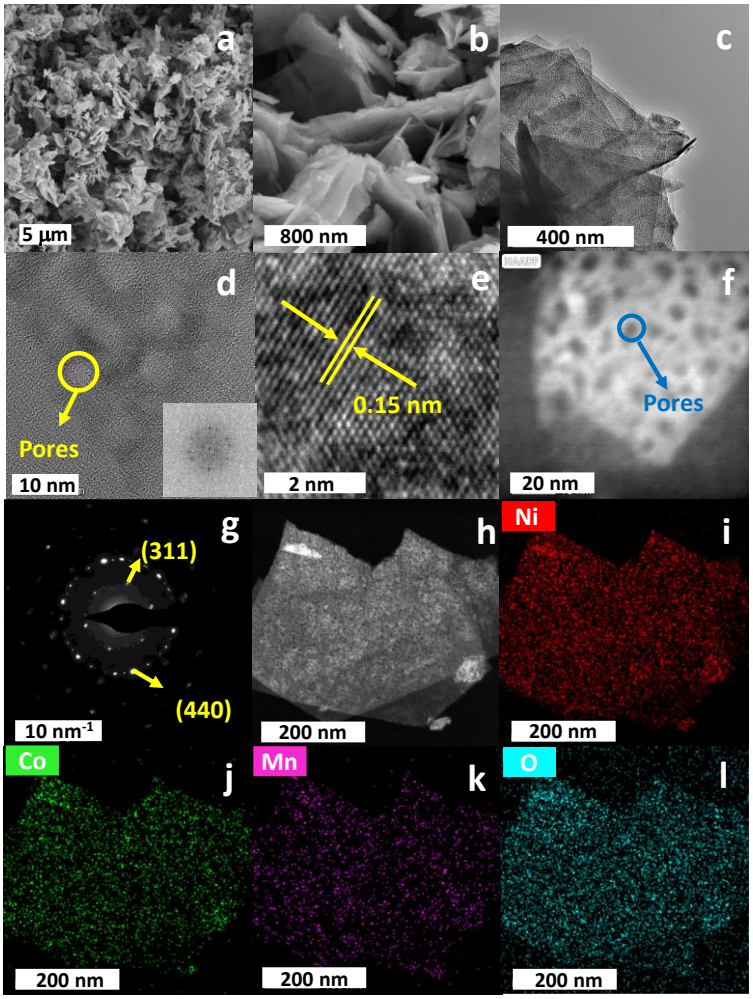

Figure 2. (a-b) SEM, (c) TEM, (d-e) HRTEM image (inset shows the FFT), (f) HAADF image, (g) SAED, (h) HAADF image and elemental mapping of (i) Ni, (j) Co, (k) Mn, (l) O for CNM.

Figures 2a and b display the low and high resolutions SEM images of CNM. The image comprises sheet-like morphology with individual sheets cross-stacked with others. Figure S2 (a-f) displays the SEM images of bimetallic CN, NM and CM. The 2D morphology of CNM is also evident from the TEM image in Figure 2c. High-resolution TEM (HRTEM) images in Figure 2d

signify the existence of pores uniformly distributed throughout the sheets. The lattice spacing in the HRTEM image was observed to be 0.15 nm (Figure 2e), which corresponds to the (440) plane of cobalt-nickel manganese oxide.[81] Inset in Figure 2d shows the corresponding Fast Fourier Transform (FFT) image where the spots signify the presence of nanoscale crystals. Figure 2f shows the high angular annular dark-field STEM images (HAADF-STEM) of another region of a sheet which further serve as proof for the existence of pores within the sheets. The ring pattern in selected area electron diffraction (SAED) reveals the polycrystalline nature of the nanosheets with the presence of the (311) and (440) planes as shown in Figure 2g.[82] Figure 2h shows the HAADF image of two overlapping sheets whose elemental mapping is presented in Figure 2(i-l). This confirms the uniform/homogeneous distribution of multi-elements (Ni, Co, Mn, and O) along with the sheets. The ratio of Ni:Co:Mn was observed to be 1.0:0.3:0.2 from Energy-dispersive X-ray spectroscopic analysis (EDS) which is consistent with that obtained from ICPMS studies. The ratio is found to be 1.0:0.33:0.22 from ICPMS studies. The elemental composition for bimetallic system was found to be 1.0:0.18 (Ni: Mn) for NM, 1.0:0.45 (Co: Mn) for CM, and 1.0:0.67 (Co: Ni) for CN.

The N_2 adsorption-desorption isotherm and pore size distribution for CNM are shown in Figure S3a and S3b. The adsorption-desorption isotherm suggests type IV isotherm. The BET surface area is estimated to be 127.094 m^2/g with average pore size of 4.08 nm is observed. This suggests high surface area that allow easy access to electrolyte.

XPS studies were carried out to analyze the surface composition and bonding state. All the peaks have been charge-corrected using C1s as the reference at 284.6 eV.[83] Figure 3a presents the XPS survey spectra and Figure 3(b-g) displays the high-resolution XPS (HRXPS) spectra corresponding to Co2p, Ni2p, Mn2p and O1s for CNM, respectively. The HRXPS of Co2p, Ni2p,

Mn2p, C1s and O1s for bimetallic (CN, CM and NM) are presented in Figure S4 and S5. The Co2p consists of two spin-orbit coupling $2p_{3/2}$ and $2p_{1/2}$, which can be deconvoluted into three bands each (Figure 3 b, c and Figure S4).[84] $Co2p_{3/2}$ for CNM consists of peaks at 779.4, 781.0, 782.7 eV, corresponding to Co^{3+}, Co^{2+} and $Co^{2+}(Co(OH)_2)$, respectively. In addition, a satellite peak was observed at 785.6 eV.[85] The satellite peak of CNM has a higher binding energy of 0.7 eV over the bimetallic oxides, suggesting that Co acts as an electron-donating site.[42,86,87] Similarly, deconvolution has been performed for Ni (Figure 3d, e and Figure S4). For CNM, Ni $2p_{3/2}$ consists of bands at 853.7, 855.3, and 856.8 eV, which correspond to Ni^{2+}, Ni^{3+}, and Ni^{2+} ($Ni(OH)_2$), together with a shakeup at 860.6 eV.[85] Mn^{2+}, Mn $^{3+}$ and Mn^{4+} were also observed in Mn $2p_{3/2}$ at 637.1, 641.7, 645.1 eV, respectively along with $Mn2p_{1/2}$ at 653.2 eV (Figure 3f).[55] It was observed that Ni2p (~0.5 eV w.r.t CN and ~0.2 eV w.r.t NM) and Mn2p (~1.1 eV w.r.t CM and ~0.6 eV w.r.t NM) experience a shift towards lower binding energy for CNM when compared to bimetallic system. This implies that these elements behave as electron-accepting sites. [42,86,87] Figure 3g and Figure S5 shows O1s spectrum consisting of three bands around 529.1, 530.7, and 532.4 eV representing lattice oxygen (O_L), surface oxygen/vacancy or defects (O_V) and chemisorbed hydroxyl or organic species (O_C), respectively.[88] The deconvoluted peaks of O1s spectra for CNM shifts towards lower binding energy when compared to bimetallic counterparts. For O_L, the shift is 0.61, 0.26 and 0.49 eV for NM, CM and CN, respectively. This suggests that the electron transfer from Co to Ni and Mn occurs via oxygen bridge.[86,89]

Overall, the XPS study confirms the presence of hybrid oxide and hydroxide components. Moreover, the study suggests that there is partial electron transfer from Co to Ni and/or Mn via oxygen bridge resulting in the shift in elemental peak position (Co2p, Ni2p, Mn 2p and O1s) for

CNM with respect to the bimetallic system. This further suggests the significant electronic modulation in the electronic structure in the trimetallic system. [90,91]

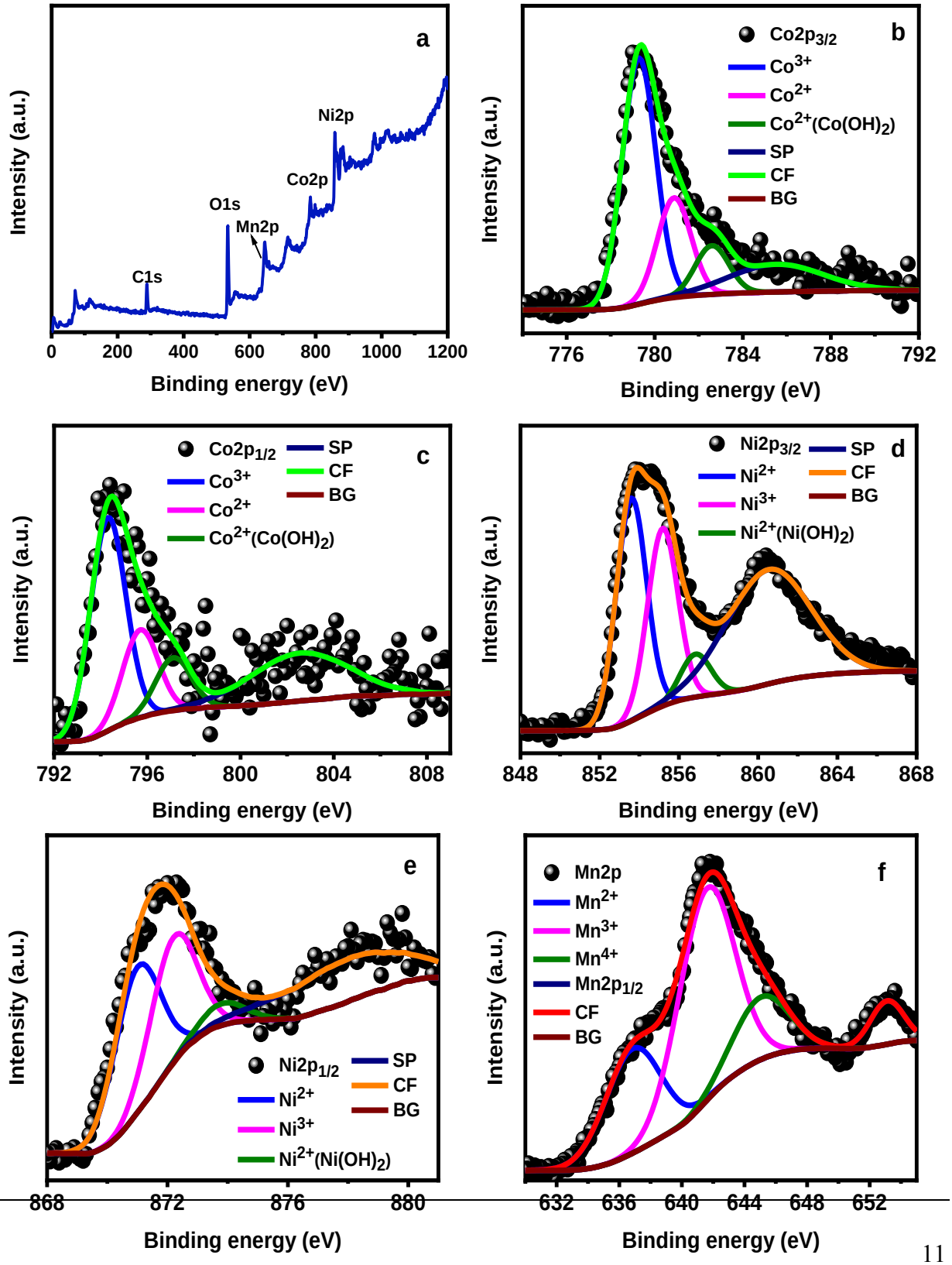

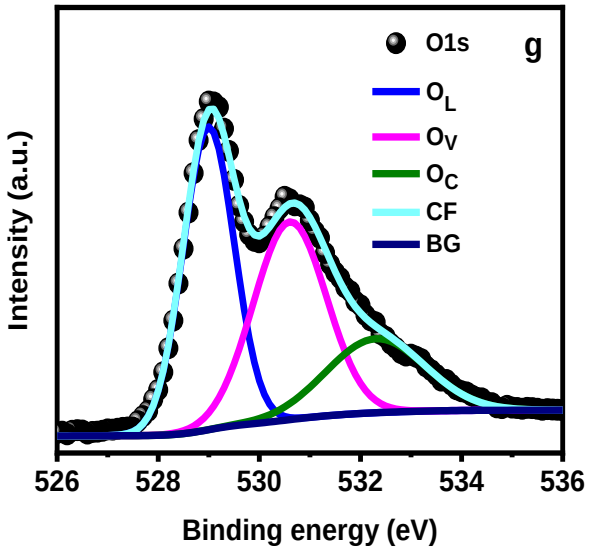

Figure 3. XPS of (a) survey spectrum (b, c) Co2p, (d, e) Ni2p, (f) Mn2p and (g) O1s for CNM (SP: satellite peak, CF: cumulative fit, BG: baseline).

To have a detailed investigation on CNM, XAS measurements were carried out. The normalized XANES spectra of CNM are shown in Figure 4 (a-c) for Co, Mn and Ni K-edge along with their respective standards. The absorption edge position of CNM at Co K-edge (Figure 4a) is coinciding with Co_3O_4 (Co^{2+}/Co^{3+}) around 7715 eV and shifted to higher energy as the absorption edge grows. This indicates the presence of a mixed oxidation state of Co ions in CNM. Similar behavior has also been observed for Mn K-edge (Figure 4b) and the absorption edge of CNM lies in between Mn_2O_3 (Mn^{3+}) and MnO_2 (Mn^{4+}). In the case of Ni K-edge (Figure 4c), the absorption spectrum of CNM is similar to NiO (Ni^{2+}). However, a small shift in energy adsorption edge (inset in Figure 4c) is observed signifying the increased average oxidation state of Ni due to the presence of Ni^{3+} on the surface.[4]

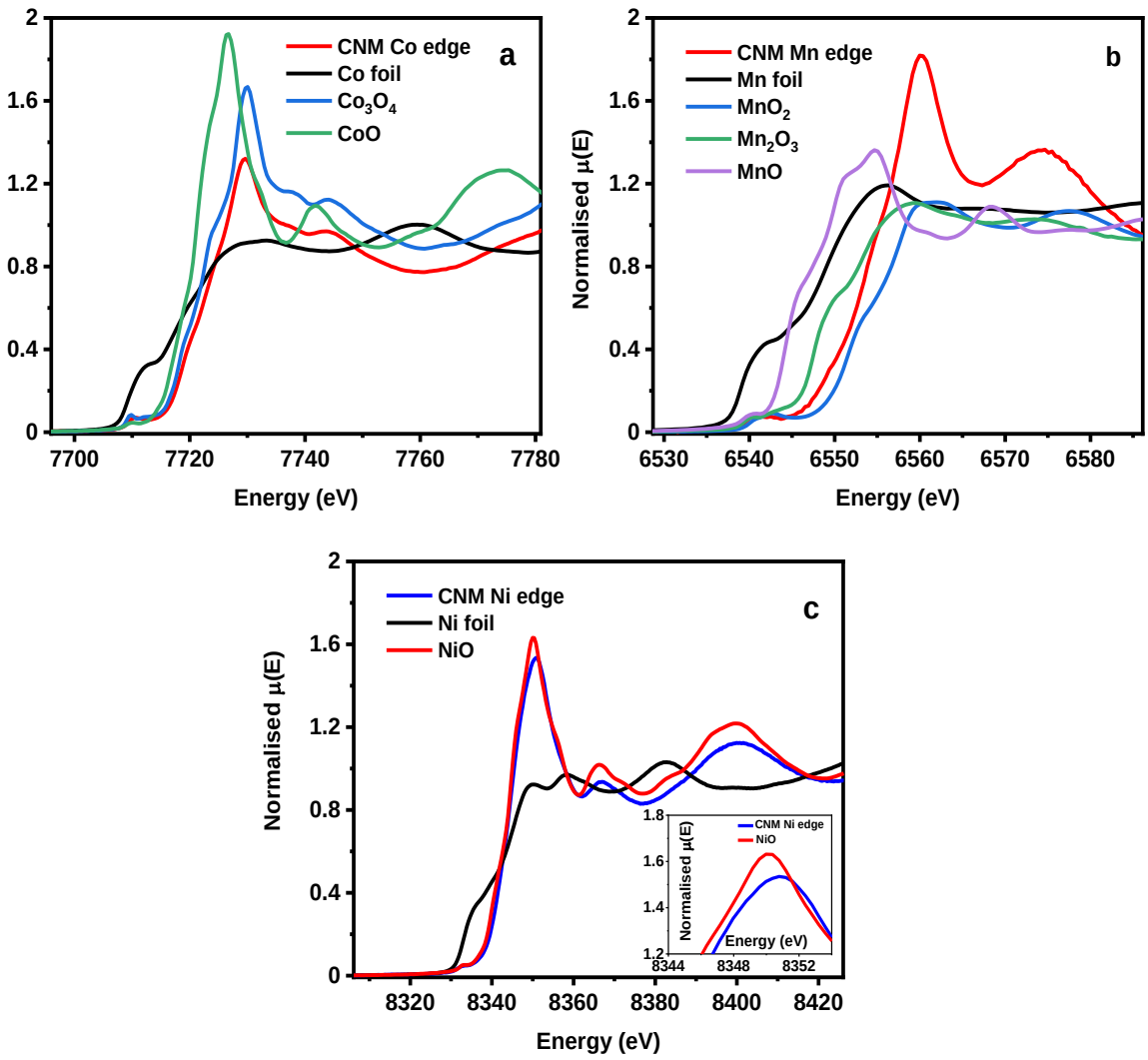

Figure 4: XANES spectra of CNM along with that of standards at (a) Co, (b) Mn and (c) Ni (inset shows the magnified region of CNM Ni edge and NiO standard) K edges.

The local structure around the absorbing atom is obtained from the quantitative analysis of EXAFS spectra [3]. The Fourier transform EXAFS spectra (χ(R) Vs R) are shown in Figure 5 along with that of the corresponding best fits. The Fourier transform spectra shown in Figure 5 are phase uncorrected, hence showing the coordination peak at relatively lower distances compared to actual bond lengths. The Fourier transform range of 3-11 $Å^{-1}$ and fitting range of 1-3 Å are used for all three absorption edges. The amplitude reduction factors have been obtained from their respective

metal standards. The fitting results are shown in Table S1. The first peak around 1.5 Å is the contribution of metal-oxygen (M-O). This metal -oxygen bond length is relatively larger for Ni-O compared to Co-O and Mn-O. The second peak around 2.5 Å is the contribution of M-M scattering and this bond length is similar for all three absorption edges. The scatterer responsible for the second peak cannot be differentiated between Ni, Mn and Co due to similar scattering factors of nearby atomic numbers.

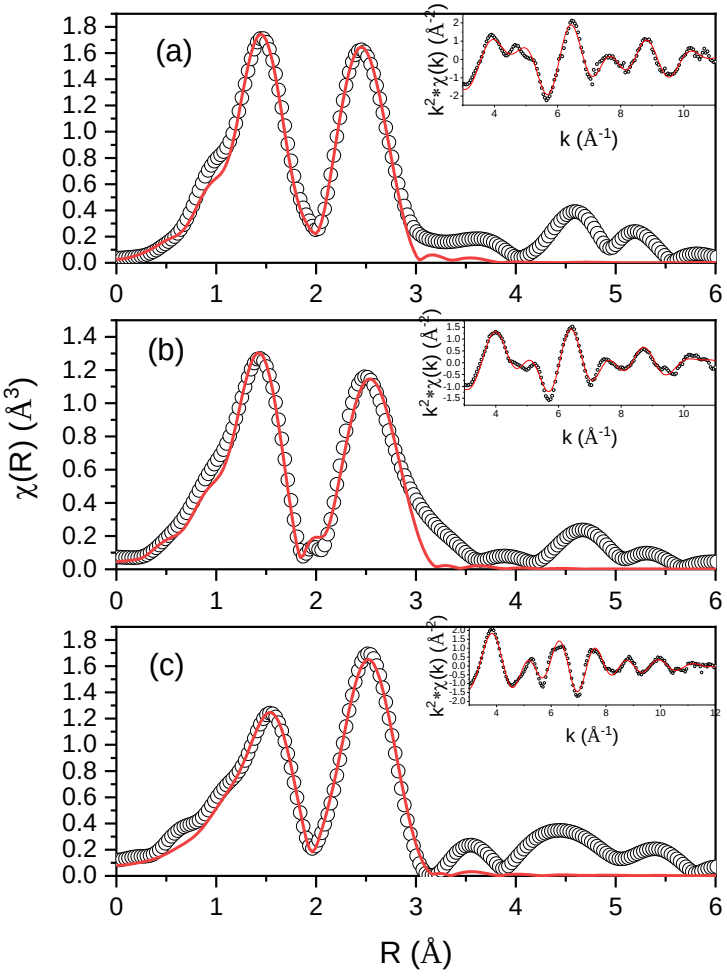

Figure 5: Fourier transformed EXAFS spectra of CNM at (a) Mn, (b) Co and (c) Ni K-edge where the experimental spectrum is represented by scattered points and theoretical fit is represented by solid lines. The inset of each figure shows corresponding k-space spectrum and its fitting.

3.1 Oxygen electrochemistry:

To study the potential applicability of the electrocatalyst in the water oxidation reaction, linear sweep voltammetry (LSV) measurements were carried out at a rotation speed of 1600 rpm and a scan rate of 5 mV/s.

Loading optimization for CNM is shown in Figure S6. At lower catalyst loading on glassy carbon electrode, the number of the active site of the catalyst is limited, which has resulted in the low OER performance. With the increase in loading (until optimized loading is achieved at 0.22 mg/cm^2), the number of active sites increases leading to an increase in OER activity. Further increase in the loading hinders activity due to delay in electronic communication between the glassy carbon electrode and electrocatalyst.[61,93] The OER polarization curves for CNM, NM, CM, CN, and RuO_2 for the optimized catalyst loading (@ 0.22 mg/cm^2) are presented in Figure 6a. The iR-corrected OER curves are presented in the inset. Current density measurements can contribute from both catalysis and material corrosion. Corrosion occurs when transition metals undergo electrochemical dissolution. According to E-pH diagram, transition metal oxides/ (oxy)hydroxides are thermodynamically stable at $pH \geq 7$ in anodic potential. [83] As a result, they are often used as the passivation layer to prevent corrosion of various transition metal based non-oxide catalysts in OER.[94] Therefore, the contribution from material corrosion in the current density can be ignored in our study. Figure S7 and 6b compare the onset and overpotential for these electrocatalysts. It was observed that the trimetallic system shows enhanced activity with a

low onset (247 mV @ 2 mA/cm^2) and overpotential (287 mV/s @ 10 mA/cm^2), which compare favorably with the commercially available OER catalyst, RuO_2. The onset and overpotential were observed to be lowest for CNM and highest for CN (CNM < NM < CM < CN). The overall performance of our electrocatalysts is presented in Table 1. Figure 6c shows the Tafel slope, which is low for CNM suggesting that trimetallic nanosheets offer the best OER kinetics. The performance comparison with the reported trimetallic system is presented in Figure 6d and Table S2. The Faradaic efficiency of the electrocatalyst is estimated using the RRDE setup as described in the supplementary information.[95–97] The highest Farradaic efficiency of 99.93 % is achieved at an applied potential of 1.496 V vs RHE (Figure 6e). At higher disk potential, Faradaic efficiency decreases due to the rise in undissolved oxygen bubbles that hinder efficient collection by the Pt ring electrode. The decrease in Faradaic efficiency with increasing disk potential has also been reported earlier.[95,96] Further, the amount of oxygen evolved at 1.496 V vs RHE is evaluated using the Equation 1 and presented in Figure S8.[98]

$$N_{O_2}\,(\mathrm{mol}) = \frac{\eta_F \times I\,(A) \times t\,(s)}{4 \times 96485\,(C\,mol^{-1})} \qquad (1)$$

Where, η_F and I signify Faradaic efficiency and current at 1.496 V vs RHE, respectively; t is time.

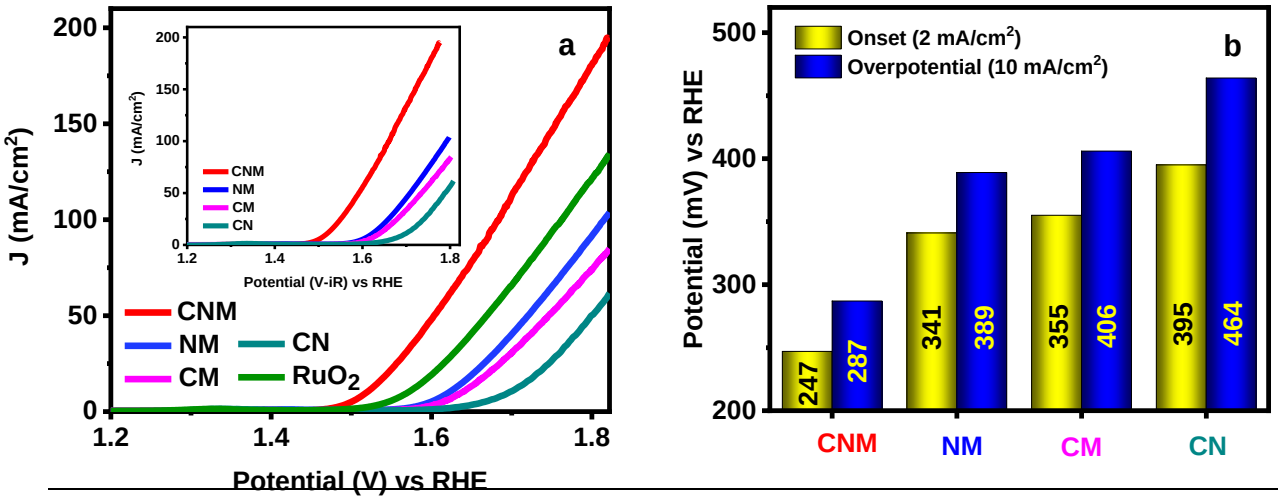

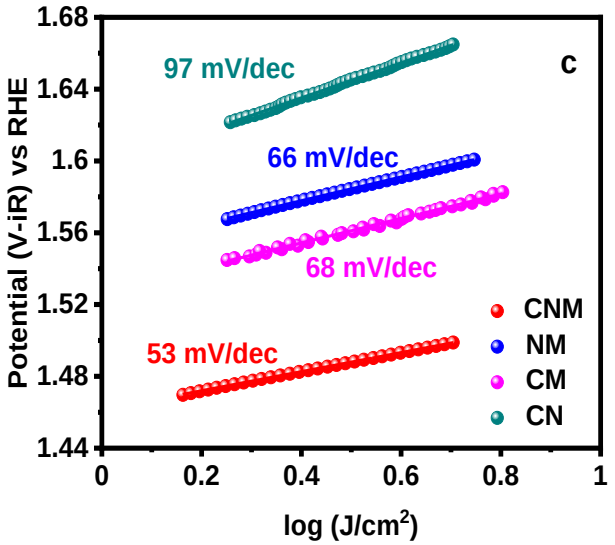
c
97 mV/dec
66 mV/dec
68 mV/dec
53 mV/dec
CNM
NM
CM
CN
Potential (V-iR) vs RHE
log (J/cm2)

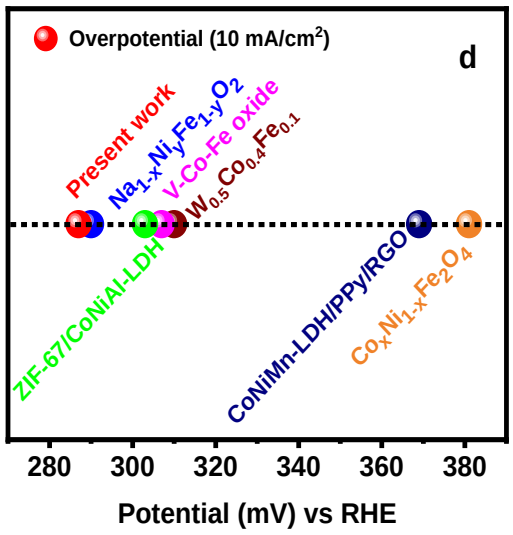
d
Overpotential (10 mA/cm2)
Present work
Na1-xNiyFe1-y-O2
V-Co-Fe oxide
W0.5Co0.4Fe0.1
ZIF-67/CoNiAl-LDH
CoNiMn-LDH/PPy/RGO
CoxNi1-xFe2O4
Potential (mV) vs RHE

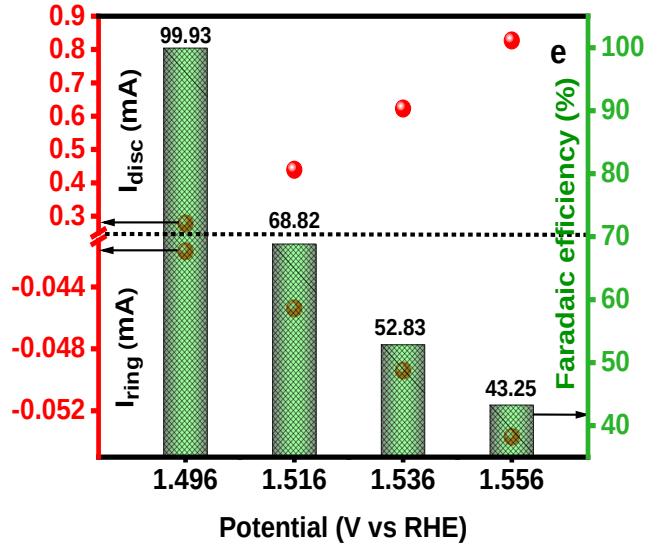
e
99.93
68.82
52.83
43.25
Idisc (mA)
Iring (mA)
Faradaic efficiency (%)
Potential (V vs RHE)

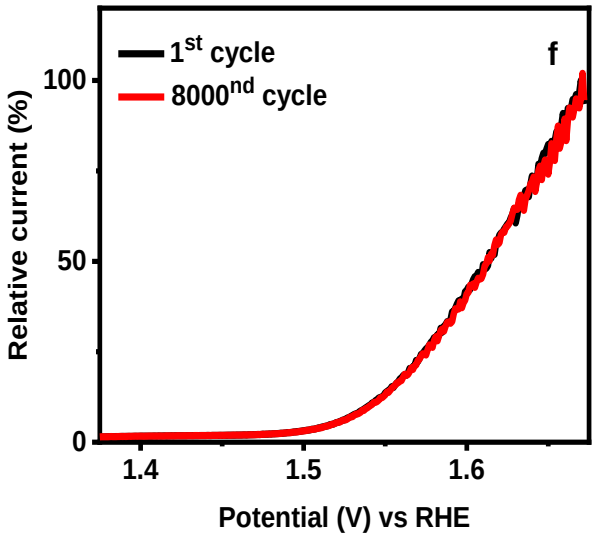
f
1st cycle
8000nd cycle
Relative current (%)
Potential (V) vs RHE

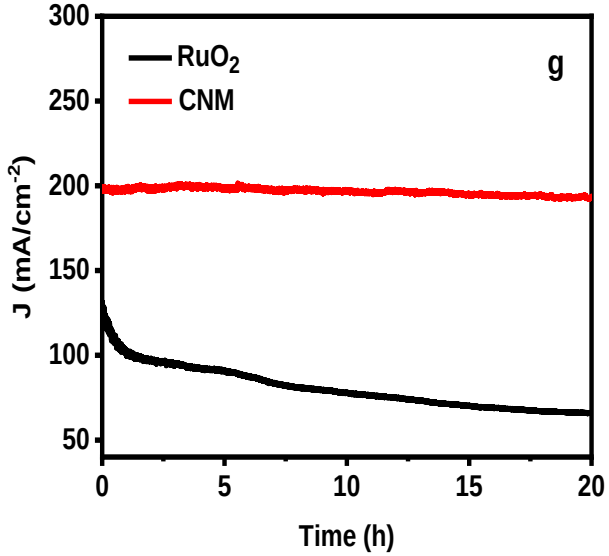
g
RuO2
CNM
J (mA/cm-2)
Time (h)

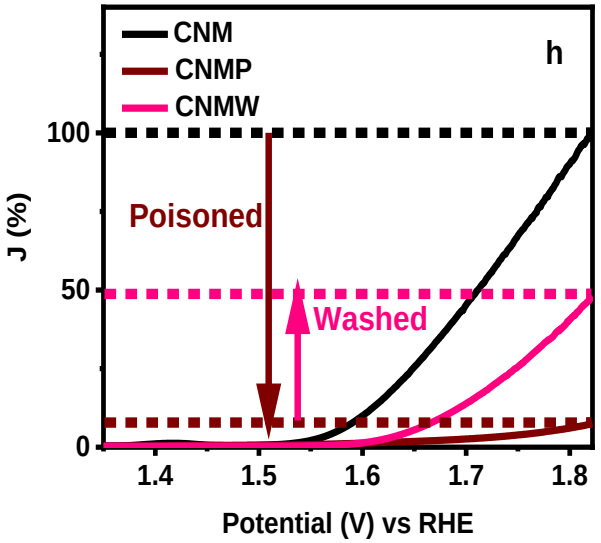
h
CNM
CNMP
CNMW
Poisoned
Washed
J (%)
Potential (V) vs RHE

Figure 6. (a) OER polarization curve without iR correction and with iR correction (inset), (b) onset and overpotential for iR corrected OER curve and (c) Tafel slope for CNM, NM, CM and CN, (d) comparison with the recently reported trimetallic system, (e) Faradaic efficiency (f) AST, (g) chronoamperometric study, and (h) poisoning study (CMNP: poisoned CNM and CNMW: poisoned samples washed) for CNM.

Table 1. Performance of all the electrocatalysts.

Electrocatalyst	η_2(mV)	η_{10}(mV)	Tafel slope (mV/dec)
CNM	**247**	**287**	**53**
NM	341	389	66
CM	355	406	68
CN	395	464	97

Figure 6f shows the accelerated stability test (AST) in the potential range of 1.25-1.65V for 8000 cycles where no significant change in current density profile was observed, signifying the excellent operational stability after the catalyst is activated. To evaluate the practical application of CNM, the chronoamperometric study (I-t measurement) is performed at 1.822 V (J ~ 200 mA/cm^2) and the results are provided in Figure 6g. Only ~3 % decrease was observed after 20 h of electrolysis. For comparison, the chronoamperometric measurement was also carried out for RuO_2. Close to 50 percent decrease in current density was observed for RuO_2 after 20 h (Figure 6g) of electrolysis whereas negligible change (~3 percent) was observed for CNM. This reveals the appreciable durability of CNM, which can be potentially used for practical electrocatalytic water splitting.

The morphology and structure of the electrocatalyst were evaluated after the durability test. The SEM image shown in Figure S9 and TEM images shown in Figure S10 (a, b) reveal that the sheet-like morphology is retained after long-term electrolysis. Figure S10c represents the HRTEM image of the post electrolysis with d-spacing of 0.479 nm which closely resembles (111) phase of Ni-Co oxide.[99] The XRD result presented in Figure S11 signifies that MOOH (M: Co/Ni/Mn) is formed. It is well accepted that transition metal oxide/hydroxide converts into more active MOOH during oxygen evolution reaction. [100] The formation of MOOH, which has a higher oxidation state is further verified by the positive shift in high-resolution XPS spectra of Co, Ni and Mn presented in Figure S12.[66]

The OER activity is also checked in 0.1 M NaOH and presented in Figure S13a. At low NaOH concentration, OER performance decreases due to increase in energy barrier which results in poor reaction kinetics. Figures S13b represents the linear sweep voltammetry (LSV) measured in OER potential regime at neutral media (pH 7). It is observed that the OER performance of CNM in neutral media is much inferior to that of alkaline condition. This signifies the suitability of CNM for OER in alkaline media.

To illustrate the importance of metal nanocentres, a poisoning study was carried out in 10 mM cyanide environment. As shown in Figure 6h, the current drastically decreased by 92.5 %. This suggests that metals interact with the highly electronegative CN^- resulting in the muting effect of the active sites.[101,102] Moreover, the onset potential increased by 36% in 40 cycles (@ 1.822V) when the catalyst was subjected to cyanide solution. Cyanide with highly active electronegative CN^- moieties bind with metal atoms or ions to form metal cyanide complex. [103] Increase in adsorption energy (ΔE_{ads}) of reactive species or reaction intermediates on the active sites for the cyanide modified electrocatalysts was observed for ORR. [102] Therefore, it is likely that the

adsorption energy of the reactant species/intermediates (O*/OOH*) increases for the cyanide modified catalyst for OER. Besides, the increase in charge transfer resistance (R_{ct}) after the poisoning is observed from the Nyquist plot in Figure S14. Therefore, the increase in onset potential can be ascribed to the deterioration in the intrinsic activity when the catalyst is subjected to cyanide poisoning.

Repeated washing of the electrocatalyst with DI water leads to the slow recovery of the catalyst performance. Ni-cyanide are weakly complexed cyanide.[104] When washed with DI water (by rotating the electrode in water), these cyanide complexes undergo dissociation and releases free cyanide into the water, [104] leaving behind the metal ions available for water oxidation.[61] Hence, repeated washing of the electrocatalyst with water leads to recovery of the catalyst performance.

3.2 Mechanistic investigation:

OER performance is governed by extrinsic activity (electrochemically active surface area, ECSA) and intrinsic activity (conductivity, reaction kinetics and adsorption energy of reaction intermediates). To understand the root cause behind the better OER performance by CNM, firstly double-layer capacitance (C_{dl}) is deduced from cyclic voltammetry (CV in Figure S15) curve in the non-faradaic region (Figure 7a) to obtain ECSA. The C_{dl} was observed to be maximum for CNM. This suggests that CNM has the largest number of electrochemical active sites for water oxidation as electrochemical surface area is directly proportional to C_{dl}.[105–108] This is also evident from the ECSA calculated from the relation presented in Equation 2 and is found to be 1.40, 1.23, 1.31 and 1.35 cm^2 for CNM, NM, CM and CN, respectively. ECSA is given by

$$\mathrm{ECSA} = \frac{C_{dl}}{C_s} * S \qquad (2)$$

where C_s represents the standard capacitance of the atomically flat surface per unit area (0.04 mF/cm^2) under the same experimental conditions and S is the geometric surface area.

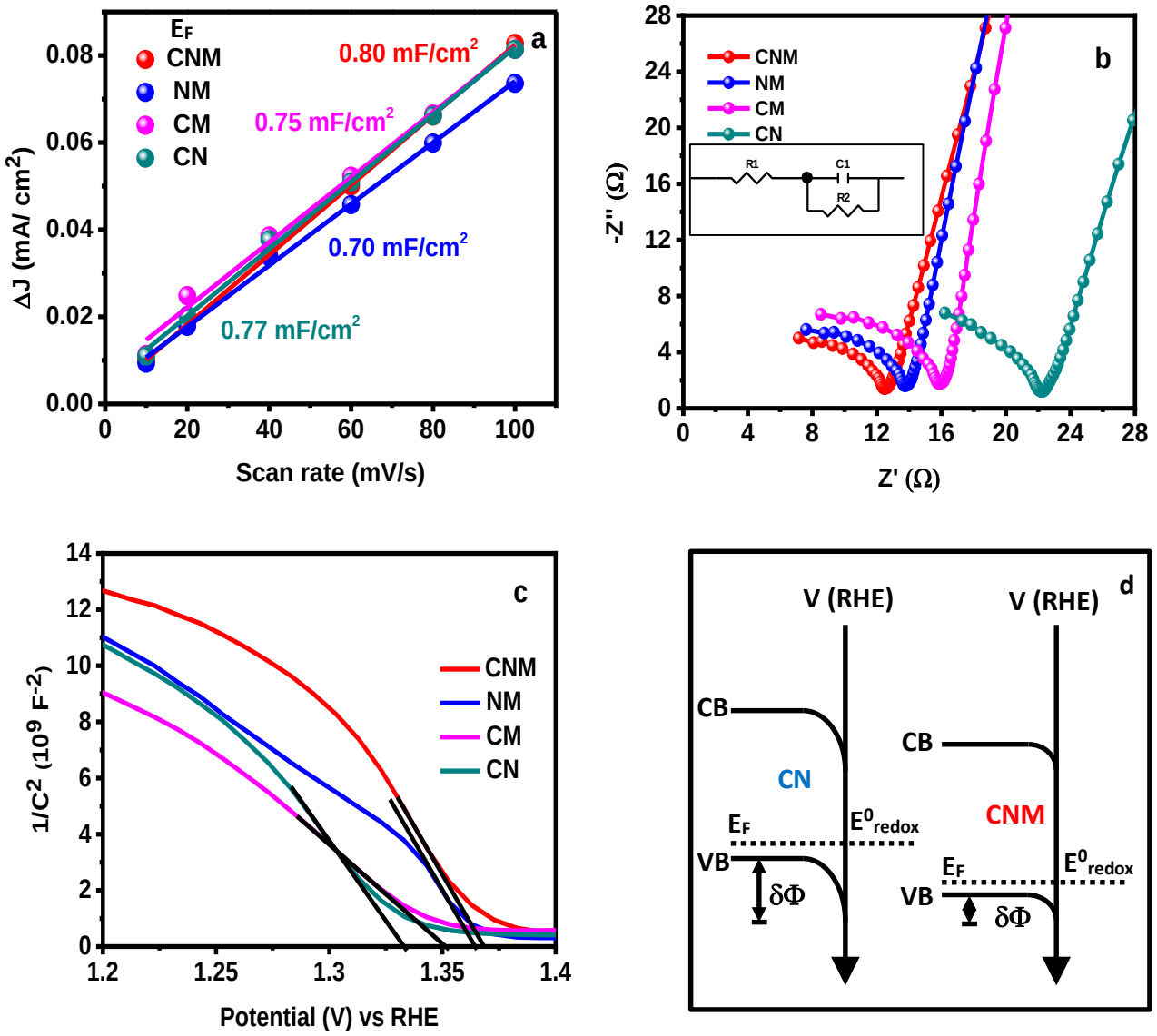

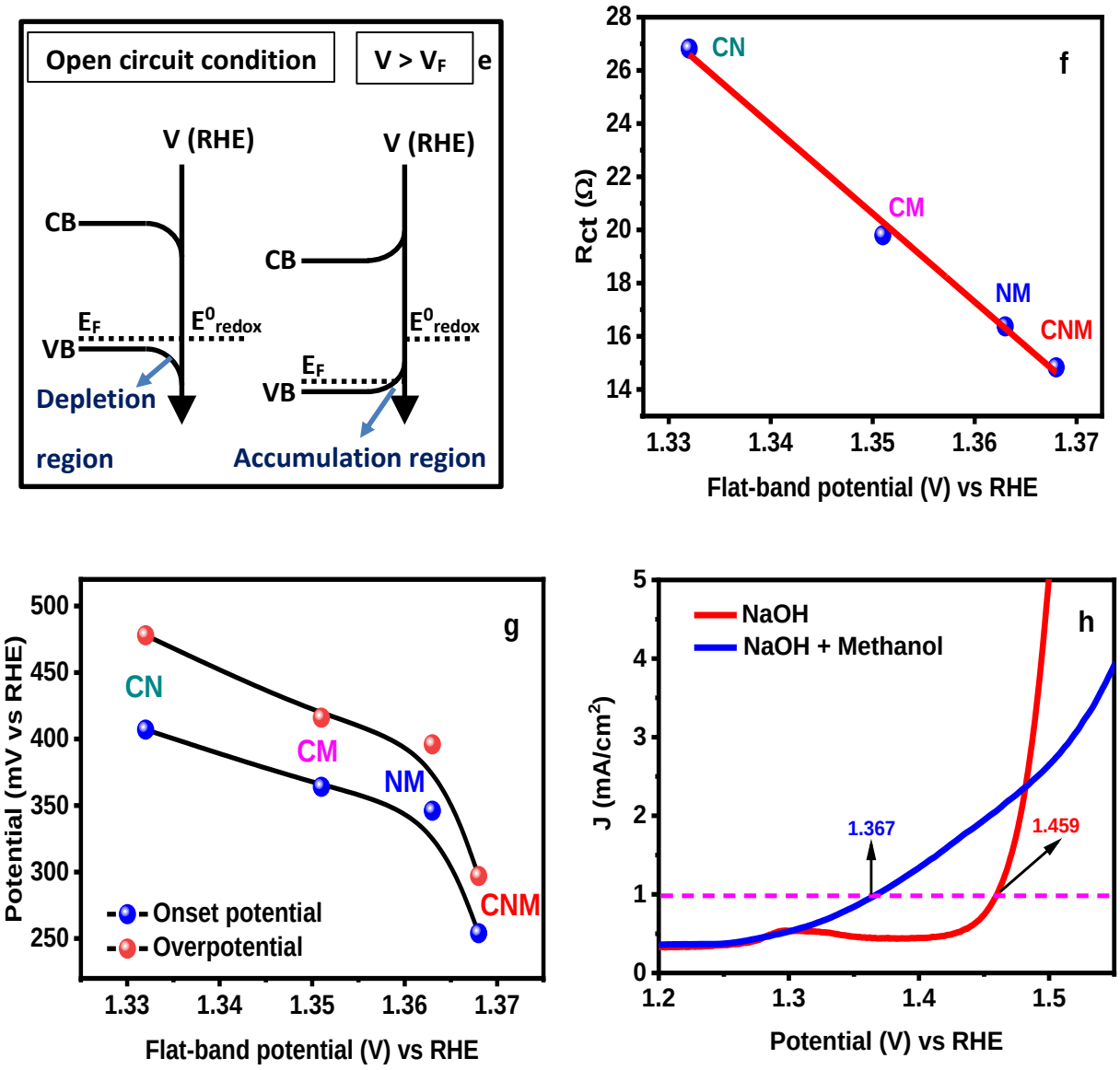

Figure 7. (a) Double-layer capacitance (C_{dl}), (b) Nyquist plot (inset shows the equivalent circuit for CNM, where R1 is solution resistance and R2 is charge transfer resistance (R_{ct})), (c) Mott-Schottky plot, (d) energy band diagram for CN and CNM, (e) energy band diagram at open circuit condition and $V > V_F$ for p-type semiconductor, (f) R_{ct} vs flat-band potential, (g) C_{dl} normalized onset and overpotential vs flat-band potential and (h) OER polarization curve measured in 1M NaOH and 1M NaOH + 1 M methanol.

Impedance studies were carried out to investigate the interface behavior. Figure 7b presents the Nyquist plots for the as-synthesized electrocatalysts (inset shows the equivalent circuit for CNM). The charge transfer resistance followed the order of CNM < NM < CM < CN, which agrees with the OER performance.

To have an insight on the charge transfer behavior, Mott-Schottky analysis was carried out to determine the flat-band potential. Mott-Schottky model gives the capacitance at the space-charge region (C) and is related to the flat-band potential via Equation 3 (p-type semiconductor). The negative slope in Figure 7c signifies the p-type behavior for all the electrocatalyst. The intercept on the x-axis gives the flat-band potential.

$$\frac{1}{C^2} = \frac{2}{\epsilon\epsilon_0\ eA^2N_A}\left(V - V_F - \frac{kT}{e}\right) \quad (3)$$

where ϵ is dielectric constant, ϵ_0 is vacuum permittivity, e is charge of the electron, A is the surface area of the electrode, N_A is acceptor density, V is applied potential and V_F is the flat-band potential. The flat-band potential is the potential of the semiconductor band (valence band for p-type) edge measured against a reference electrode in the solution when no band bending occurs.

In a semiconductor-electrolyte junction, band bending occurs so that both the Fermi level lies in the same energy level (Figure 7d). A region is formed at the semiconductor surface that is depleted of the majority charge carrier (equilibrium condition). The amount of band-bending (built-in-potential/ potential barrier) is given by $\delta\phi = V\text{-}V_F$, where V and V_F represent the applied and flat-band potentials, respectively.[109] When a positive potential is applied to a p-type semiconductor (equilibrium is disturbed), the potential barrier is reduced and the charge carrier starts to flow from semiconductor to electrolyte. When a potential greater than flat-band potential is applied, energy

levels rearrange so that an accumulation region is formed (Figure 7e). As this layer is rich in charge carrier, efficient charge exchange between semiconductor and electrolyte followed by surface reaction occurs. Therefore, a smaller δø makes it easier to start a reaction.[109] In other words, higher flat-band potential signifies more positive redox potential. This would lead to a higher affinity of the semiconductor towards electrons and result in efficient charge transfer at the electrode-electrolyte interface. Interestingly, the flat-band potential presented in Figure 7f follows the order CN < CM < NM < CNM, which agrees with the charge transfer resistance. The charge density was also calculated from the slope of the Mott-Schottky plot (assuming same A and for all the electrocatalyst) and is normalized with that of CM presented in Figure S16. Though the charge density obtained was low for CNM, its better OER activity signifies the importance of flat-band potential in the OER kinetics. The above explanation can also be justified using Equation 4, which indicates that the surface carrier concentration (p_s for p-type semiconductor) depends on the acceptor concentration in the bulk (p, built-in-potential (δø), and applied potential (V).[110]

$$p_s = p\exp[-e(\delta\text{ø} - V)/KT] \quad (4)$$

The present study suggests that the low built-in-potential acts as a driving force resulting in a higher surface charge concentration available for reactions. In other words, the low built-in potential leads to a higher probability of hole transfer from semiconductor to the electrolyte for CNM.

The best conductivity of CNM is also evident from the quasi-reversible $[Fe(CN)6]^{3-/4-}$ redox study presented in Figure S17. The current is maximum and redox peak separation ($\Delta E = E_O - E_R$, E_O = oxidation potential and E_R = reduction potential) is minimum for CNM, suggesting its better reversibility and easier charge transfer at the interface. Hence, the highest flat-band potential

results in a better electronic conductivity (minimal charge transfer resistance), minimal onset and overpotential for CNM. Figure 7f and Figure S18 present a linear dependency of charge transfer resistance and Tafel slope on the flat-band potential that signifies the importance on the OER kinetics. The study suggests that intrinsic activity is governed by conductivity (kinetics) and adsorption energies of OER intermediates (thermodynamics).[36] To visualize the impact of flat-band potential on intrinsic activity, onset and overpotential (calculated after iR correction followed by normalizing with ECSA) is plotted with respect to the flat-band potential. The onset/overpotential was observed to decrease with increasing flat-band potential (or decrease in charge transfer resistance) while a sudden drop was observed in the case of CNM (Figure 7g). Moreover, the onset potential, overpotential, and charge transfer resistance decrease with an increase in flat-band potential, following a similar trend for the adsorption energy. When a metal is in contact with an electrolyte, most of the potential drops at the interface occur in the Helmholtz region (electrolyte phase). It may be noted that potential drop occurs in both the semiconductor and solution side across the semiconductor-electrolyte junction. In the semiconductor side, the potential drop occurs in the space charge region and leads to band bending, while the potential drop occurs in Helmholtz and Gouy-Chapman layer in the solution side. As our electrochemical measurements were carried out in 1 M NaOH, the contribution from the Gouy-Chapman layer can be ignored.[111] However, the contribution from the Helmholz layer is significant at accumulation condition when the applied potential is greater than flat-band potential ($V>V_F$) and the potential drop shifts from space charge region to the Helmholz layer. Therefore, electrocatalysts with optimum adsorption energy for ions (OH^-/reaction intermediates) are beneficial for enhanced OER performance.

It is also understood that the three-component system reduces the overpotential by preventing the extreme adsorption of intermediate species like OH, O and OOH.[36,43,59,112] Introduction of high valence state elements is proven to improve the OER performance by optimizing the adsorption energy of reaction intermediates. [66] Therefore, the sudden dip in onset potential/overpotential for CNM in Figure 7g can be ascribed to the reduced energy barrier for reactant species or intermediates in addition to minimal charge transfer resistance.

The widely accepted OER mechanism is the Adsorbate evolution mechanism (AEM) and the corresponding reaction steps are given in Equation 5 to 8.[113]

$$OH^- + * \rightarrow HO^* + e^- \quad \text{(Step 1)} \tag{5}$$

$$HO^* \rightarrow O^* + e^- + H^+ \quad \text{(Step 2)} \tag{6}$$

$$O^* + OH^- \rightarrow HOO^* + e^- \quad \text{(Step 3)} \tag{7}$$

$$HOO^* \rightarrow * + O_2 + e^- + H^+ \quad \text{(Step 4)} \tag{8}$$

Therefore, the intermediate for OER includes HO*, O*, and HOO*. In AEM, $\Delta G_{O^*} - \Delta G_{HO^*}$ (difference in adsorption energies of *O and *OH) is the descriptor that is used in predicting the OER activity.[69,113] The equilibrium potential for steps 1, 2, 3 and 4 are E_1^0, E_2^0, E_3^0 and E_4^0, respectively and presented by Equation S2 to S5. The overpotential is sum of all the elementary steps.

Methanol oxidation reaction (MOR) is proven to be a reliable method to probe the OH*.[114] MOR for CNM is carried out and the result is presented in Figure 7h. Methanol reacts with electrophilic OH* and form aldehydes. Therefore, the onset potential ($V_{NaOH+methanol}$ at ~ 1 mA/cm^2) of MOR that signifies the adsorption potential of OH* intermediate is found to be 1.367

V vs RHE for CNM. In Figure 7h, as the onset of the MOR lies before that of OER (V_{NaOH} = 1.459 at 1 mA/cm^2) signifies that the second elementary step that transform OH* to O* is the rate determining step. It is also proposed that, if step 2 is the rate determining step, the potential corresponding to OER onset potential is required to transform OH* to O*. Therefore, the adsorption energy of OH* and O* is 1.367 and 2.826 eV, respectively.

According to the Sabatier principle, the binding of the reaction intermediates should be optimum for efficient reaction. One of the strategies to regulate the electronic structure to have an optimized $\Delta G_{O^*} - \Delta G_{HO^*}$ is to introduce a foreign element. It is realized from various reports that when 3d transition metals with high valence states (like V or Cr) are incorporated into Ni/Fe/Co based binary oxides or hydroxides, the M (M: V or Cr) sites are seen to have short M-O and optimum binding strength for OER intermediates, hence serve as the active sites [115][86]

Besides, the best oxygen evolution electrocatalyst should have e_g occupancy of 1.2 which signifies effective adsorption of reactant molecules/intermediates. e_g occupancy of 0 implies too strong whereas that of 2 signify too weak bonding with adsorbed oxygen species. Ni^{3+} and Mn^{3+} have $t_{2g}^6e_g^1$ and $t_{2g}^3e_g^1$ i.e e_g orbital occupancy close to unity [103] whereas Co^{3+} has $t_{2g}^6e_g^0$. Doping high valence transition (3d, 4d or 5d) metals stabilize the active state of 3d metals (eg. Ni^{3+} for Ni). [116,117] They tends to withdraw electrons from the active 3d metals and allow them to stay in their high valence state (eg. Ni^{3+} for Ni) that are considered active sites for OER.

It is understood that shorter M–O bond is beneficial from the adsorption of OER intermediates. [118,119] From the EXAFS analysis, it is evident that the Co-O (1.91±0.02 Å) and Mn-O (1.92±0.01 Å) has shorter bond length compared to Ni-O (2.05±0.01 Å). Further, from the HRXPS analysis of sample post OER (Figure S12), the significant shift towards higher binding energy for

Mn and Co was observed which is an indication of shrinkage of Mn-O and Co-O bond-length during OER.[86,115] This signifies that Mn and Co get activated for participation in the OER.[86,92,115,120] Subsequently, a relatively small shift in peak position to higher binding energy for Ni (Ni^{2+}) is visible. This suggest that Mn being high valence element can stabilize the Ni^{3+} and maintain the optimum adsorption of reaction intermediates for OER.[67] Therefore, Mn, Co and Ni can synergistically promote OER in CNM.

In order to understand the kinetics of OER, polarization curves were obtained at different temperature to calculate activation energy (E_a) . E_a signifies the kinetic barrier for the reaction which is calculated using Arrhenius equation (Equation 9).[102,113]

$$\ln\ (J) = \ln\ (A) - \frac{E_a}{R}\left(\frac{1}{T}\right) \quad (9)$$

Where J = magnitude of current density at 1.822 V vs RHE, A = exponential factor, R = Gas constant = 8.314 J mol^{-1} K^{-1}, T = Absolute temperature in Kelvin. Detailed calculation of E_a has been presented in Supplementary information.

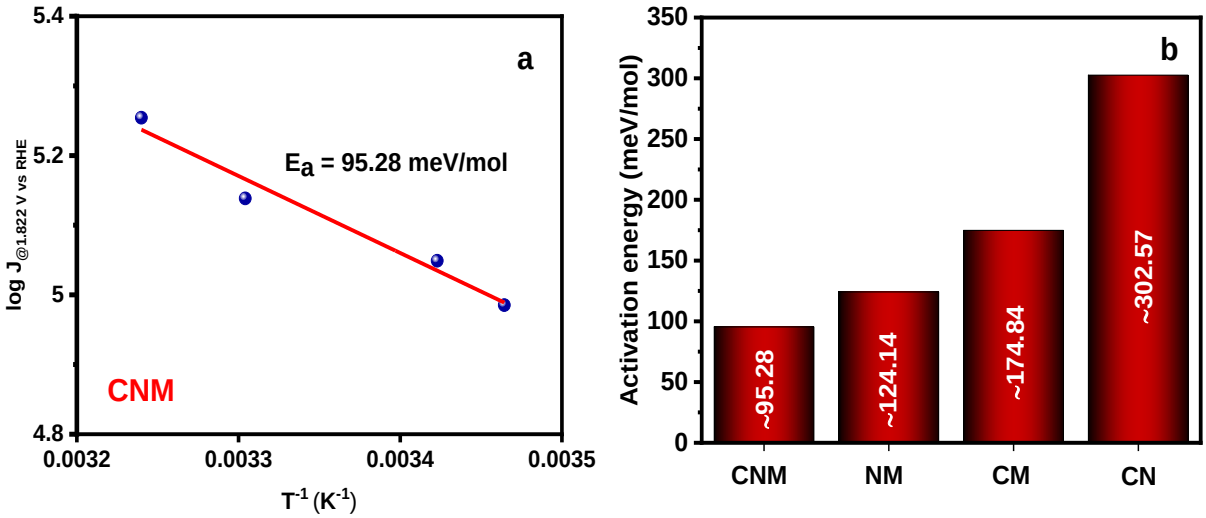

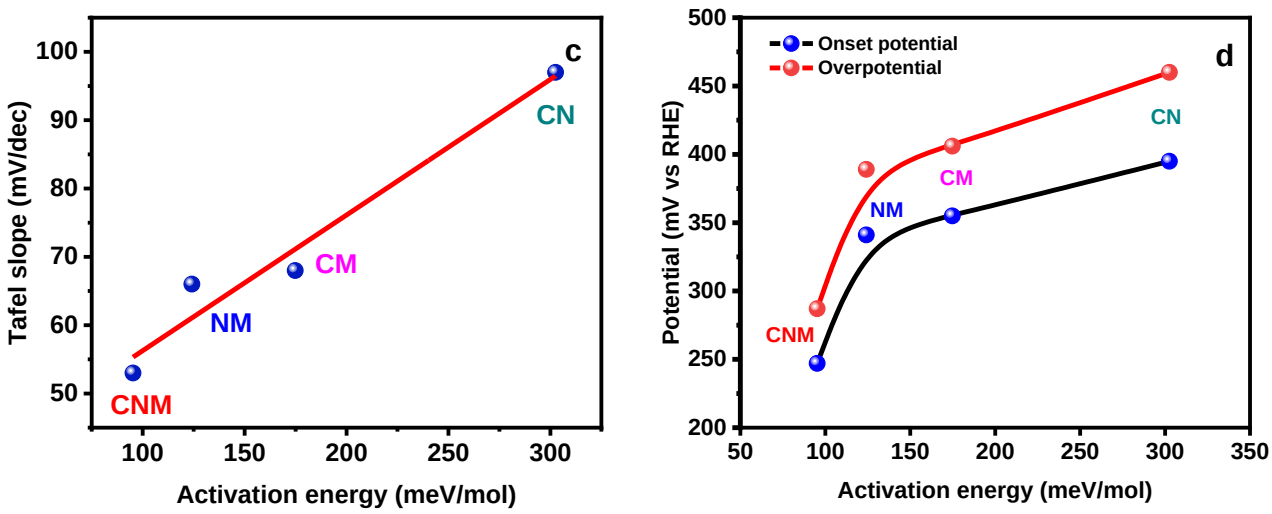

Figure 8. (a) Arrhenius plot for CNM, (b) E_a, (c) Tafel slope vs E_a and (d) onset potential and overpotential vs E_a for CNM, NM, CM and CN.

Figure 8a and Figure S19 represents Arrhenius plot for all the electrocatalysts and the obtained E_a has been summarized in Figure 8b. The lowest E_a observed for CNM signifies the presence of active sites with higher catalytic activity due to minimum kinetic barrier for OER. Figure 8c gives a linear correlation between the Tafel slope (a parameter signifying reaction kinetics) and E_a.

To realize the impact of E_a on the intrinsic activity, the onset potential and overpotential as a function of E_a is plotted that reveals a linear correlation for the bimetallic system whereas a sudden decrease in the onset and overpotential for CNM was observed. This validates the improved OER activity for the trimetallic system over the bimetallic counterparts due to superior reaction kinetics which is a measure of intrinsic activity.

We have also evaluated kinetic parameters such as exchange current density (J_0), transfer coefficient (α), and forward rate constant (k_f).[122–124] The details of the procedure is presented

in the supplementary information. The exchange current density implies the current flowing per unit area in both directions between the electrode-electrolyte at equilibrium. The J_0 for CNM (obtained from Figure S20) is 4.443×10^{-5} mA cm^{-2}. Transfer coefficient defines the reaction's direction and is between 0 to 1 where $\propto$ value of 0 signifies reactant like whereas 1 implies product like. The value of $\propto$ evaluated using Equation S8 is ~ 1. The k_f for CNM is presented in Figure S21c (obtained from Figure S21a,b) . The k_f at various overpotentials for CNM have been found to be in the range ~10^{-3} -10^{-2} $cm^{-1}s^{-1}$.

Overall, the study proves that trimetallic cobalt, nickel, and manganese oxide-hydroxide nanosheets possess superior water oxidation performance due to the presence of a higher number of electrochemically active sites and better intrinsic activity (better conductivity and reduced energy barrier).

4. Conclusion

In the present work, we have synthesized cobalt-nickel and manganese oxide-hydroxide porous nanosheets via a simple hydrothermal route. The role of intrinsic activity on their electrochemical performance has been clarified. The study concludes that the position of flat-band potential plays a significant role in determining the OER activity. High flat-band potential is responsible for reduced charge transfer resistance or better conductivity at the electrode-electrolyte interface. Introducing third element results in reduction of kinetic energy barrier for water oxidation. These in turn lowers the onset and overpotential. In this study, the trimetallic nanosheets offer the best OER activity due to the presence of more active sites and better intrinsic activity which in turn is the consequence of higher flat-band potential and lower activation energy compared to their bimetallic counterpart. As a result, cobalt nickel and manganese oxide-hydroxide nanosheets offer

low onset and overpotential of 247 (@ 2 mA /cm^2) and 287 mV (@ 10 mA /cm^2), respectively. Mn, Co and Ni synergistically are responsible for enhanced OER activity. The trimetallic CNM has exceeded the performance by the commercially available semi-noble metal oxide, RuO_2 in terms of activity and durability. The present study not only sheds light on the impact of electronic modulation in the electrochemical water oxidation reaction but also opens up a new avenue to design efficient electrocatalysts by tuning their electronic structure.

Acknowledgment

The authors gratefully acknowledge DST-FIST (SR/FST/PSII-009/2010), India and Ministry of Education, Singapore (RG15/16, RG16/18) for the financial support. Authors are thankful to Dr. S. N. Jha for the XAS measurement and Raja Ramanna Centre for Advanced Technology (RRCAT), Indore, India for XAS measurements facility. The author would like to thank Omeshwari Yadorao Bisen for the BET measurement.

References

[1] M. Mekaroonreung, A.L. Johnson, Estimating the efficiency of American petroleum refineries under varying assumptions of the disposability of bad outputs, Int. J. Energy Sect. Manag. 4 (2010) 356–398. https://doi.org/10.1108/17506221011073842.

[2] N. Armaroli, V. Balzani, The future of energy supply: Challenges and opportunities, Angew. Chemie - Int. Ed. 46 (2007) 52–66. https://doi.org/10.1002/anie.200602373.

[3] H. Dau, C. Limberg, T. Reier, M. Risch, S. Roggan, P. Strasser, The Mechanism of Water Oxidation: From Electrolysis via Homogeneous to Biological Catalysis, ChemCatChem. 2

(2010) 724–761. https://doi.org/10.1002/cctc.201000126.

[4] Y. Zhai, X. Ren, J. Yan, S. (Frank) Liu, High Density and Unit Activity Integrated in Amorphous Catalysts for Electrochemical Water Splitting, Small Struct. 2 (2021) 2000096. https://doi.org/10.1002/sstr.202000096.

[5] K. Zeng, W. Li, Y. Zhou, Z. Sun, C. Lu, J. Yan, J.H. Choi, R. Yang, Multilayer hollow $MnCo_2O_4$ microsphere with oxygen vacancies as efficient electrocatalyst for oxygen evolution reaction, Chem. Eng. J. 421 (2021) 127831. https://doi.org/10.1016/j.cej.2020.127831.

[6] W. Wen, Y.N. Chen, S.G. Wang, M.H. Cao, J.C. Yao, Y.J. Gu, J.M. Wu, A 3D electrode of core@shell branched nanowire $TiN@Ni_{0.27}Co_{2.73}O_4$ arrays for enhanced oxygen evolution reaction, Appl. Mater. Today. 12 (2018) 276–282. https://doi.org/10.1016/j.apmt.2018.06.006.

[7] J. Joo, T. Kim, J. Lee, S. Il Choi, K. Lee, Morphology-Controlled Metal Sulfides and Phosphides for Electrochemical Water Splitting, Adv. Mater. 31 (2019) 1–23. https://doi.org/10.1002/adma.201806682.

[8] Y. Guo, T. Park, J.W. Yi, J. Henzie, J. Kim, Z. Wang, B. Jiang, Y. Bando, Y. Sugahara, J. Tang, Y. Yamauchi, Nanoarchitectonics for Transition-Metal-Sulfide-Based Electrocatalysts for Water Splitting, Adv. Mater. 31 (2019) 1–34. https://doi.org/10.1002/adma.201807134.

[9] H. Osgood, S. V. Devaguptapu, H. Xu, J. Cho, G. Wu, Transition metal (Fe, Co, Ni, and Mn) oxides for oxygen reduction and evolution bifunctional catalysts in alkaline media, Nano Today. 11 (2016) 601–625. https://doi.org/10.1016/j.nantod.2016.09.001.

[10] W.T. Hong, M. Risch, K.A. Stoerzinger, A. Grimaud, J. Suntivich, Y. Shao-Horn, Toward

the rational design of non-precious transition metal oxides for oxygen electrocatalysis, Energy Environ. Sci. 8 (2015) 1404–1427. https://doi.org/10.1039/c4ee03869j.

[11] F. Yu, H. Zhou, Y. Huang, J. Sun, F. Qin, J. Bao, W.A. Goddard, S. Chen, Z. Ren, High-performance bifunctional porous non-noble metal phosphide catalyst for overall water splitting, Nat. Commun. 9 (2018) 1–9. https://doi.org/10.1038/s41467-018-04746-z.

[12] X. Guo, Y. Xu, Y. Cheng, Y. Zhang, H. Pang, Amorphous cobalt phosphate porous nanosheets derived from two-dimensional cobalt phosphonate organic frameworks for high performance of oxygen evolution reaction, Appl. Mater. Today. 18 (2020) 100517. https://doi.org/10.1016/j.apmt.2019.100517.

[13] X. Mao, Y. Liu, Z. Chen, Y. Fan, P. Shen, Fe and Co dual-doped Ni_3S_4 nanosheet with enriched high-valence Ni sites for efficient oxygen evolution reaction, Chem. Eng. J. 427 (2022) 130742. https://doi.org/10.1016/j.cej.2021.130742.

[14] J. Huang, J. Chen, T. Yao, J. He, S. Jiang, Z. Sun, Q. Liu, W. Cheng, F. Hu, Y. Jiang, Z. Pan, S. Wei, CoOOH Nanosheets with High Mass Activity for Water Oxidation, Angew. Chemie - Int. Ed. 54 (2015) 8722–8727. https://doi.org/10.1002/anie.201502836.

[15] G. hee Moon, M. Yu, C.K. Chan, H. Tüysüz, Highly Active Cobalt-Based Electrocatalysts with Facile Incorporation of Dopants for the Oxygen Evolution Reaction, Angew. Chemie - Int. Ed. 58 (2019) 3491–3495. https://doi.org/10.1002/anie.201813052.

[16] C.H. Kuo, I.M. Mosa, A.S. Poyraz, S. Biswas, A.M. El-Sawy, W. Song, Z. Luo, S.Y. Chen, J.F. Rusling, J. He, S.L. Suib, Robust mesoporous manganese oxide catalysts for water oxidation, ACS Catal. 5 (2015) 1693–1699. https://doi.org/10.1021/cs501739e.

[17] M. Gong, Y. Li, H. Wang, Y. Liang, J.Z. Wu, J. Zhou, J. Wang, T. Regier, F. Wei, H. Dai, An advanced Ni-Fe layered double hydroxide electrocatalyst for water oxidation, J. Am.

Chem. Soc. 135 (2013) 8452–8455. https://doi.org/10.1021/ja4027715.

[18] Y.K. Kim, J.H. Kim, Y.H. Jo, J.S. Lee, J. Accepted, Precipitating Metal Nitrate Deposition of Amorphous Metal Oxyhydroxide Electrodes Containing Ni , Fe and Co for Electrocatalytic Water Oxidation, (2019). https://doi.org/10.1021/acscatal.9b02701.

[19] M.W. Louie, A.T. Bell, An investigation of thin-film Ni-Fe oxide catalysts for the electrochemical evolution of oxygen, J. Am. Chem. Soc. 135 (2013) 12329–12337. https://doi.org/10.1021/ja405351s.

[20] X. Lv, Y. Zhu, H. Jiang, X. Yang, Y. Liu, Y. Su, J. Huang, Y. Yao, C. Li, Hollow mesoporous $NiCo_2O_4$ nanocages as efficient electrocatalysts for oxygen evolution reaction, Dalt. Trans. 44 (2015) 4148–4154. https://doi.org/10.1039/c4dt03803g.

[21] S. Gupta, A. Yadav, S. Bhartiya, M.K. Singh, A. Miotello, A. Sarkar, N. Patel, Co oxide nanostructures for electrocatalytic water-oxidation: Effects of dimensionality and related properties, Nanoscale. 10 (2018) 8806–8819. https://doi.org/10.1039/c8nr00348c.

[22] M. Risch, F. Ringleb, M. Kohlhoff, P. Bogdanoff, P. Chernev, I. Zaharieva, H. Dau, Water oxidation by amorphous cobalt-based oxides: In situ tracking of redox transitions and mode of catalysis, Energy Environ. Sci. 8 (2015) 661–674. https://doi.org/10.1039/c4ee03004d.

[23] F. Lu, M. Zhou, Y. Zhou, X. Zeng, First-Row Transition Metal Based Catalysts for the Oxygen Evolution Reaction under Alkaline Conditions: Basic Principles and Recent Advances, Small. 13 (2017) 1–18. https://doi.org/10.1002/smll.201701931.

[24] C.C.L. McCrory, S. Jung, I.M. Ferrer, S.M. Chatman, J.C. Peters, T.F. Jaramillo, Benchmarking Hydrogen Evolving Reaction and Oxygen Evolving Reaction Electrocatalysts for Solar Water Splitting Devices, J. Am. Chem. Soc. 137 (2015) 4347–4357. https://doi.org/10.1021/ja510442p.

[25] W. Gao, W. Gou, R. Wei, X. Bu, Y. Ma, J.C. Ho, In situ electrochemical conversion of cobalt oxide@MOF-74 core-shell structure as an efficient and robust electrocatalyst for water oxidation, Appl. Mater. Today. 21 (2020) 100820. https://doi.org/10.1016/j.apmt.2020.100820.

[26] X. Jia, X. Zhang, J. Zhao, Y. Zhao, Y. Zhao, G.I.N. Waterhouse, R. Shi, L.Z. Wu, C.H. Tung, T. Zhang, Ultrafine monolayer Co-containing layered double hydroxide nanosheets for water oxidation, J. Energy Chem. 34 (2019) 57–63. https://doi.org/10.1016/j.jechem.2018.09.011.

[27] R. Nandan, M.Y. Rekha, R. Devi, High-entropy alloys for water oxidation : a new class of electrocatalysts to look out for, (2020). https://doi.org/10.1039/d0cc06485h.

[28] X. Li, M. Xin, S. Guo, T. Cai, D. Du, W. Xing, L. Zhao, W. Guo, Q. Xue, Z. Yan, Insight of synergistic effect of different active metal ions in layered double hydroxides on their electrochemical behaviors, Electrochim. Acta. 253 (2017) 302–310. https://doi.org/10.1016/j.electacta.2017.09.075.

[29] H. Rachna Devi, O. Yadorao Bisen, Z. Chen, K. Kar Nanda, Spatially dispersed one-dimensional carbon architecture on oxide framework for oxygen electrochemistry, Chem. Eng. J. (2021) 133649. https://doi.org/10.1016/j.cej.2021.133649.

[30] B.M. Hunter, H.B. Gray, A.M. Müller, Earth-Abundant Heterogeneous Water Oxidation Catalysts, Chem. Rev. 116 (2016) 14120–14136. https://doi.org/10.1021/acs.chemrev.6b00398.

[31] M. Gong, H. Dai, A mini review of NiFe-based materials as highly active oxygen evolution reaction electrocatalysts, Nano Res. 8 (2014) 23–39. https://doi.org/10.1007/s12274-014-0591-z.

[32] M.D. Merrill, R.C. Dougherty, Metal oxide catalysts for the evolution of O_2 from H_2O, J. Phys. Chem. C. 112 (2008) 3655–3666. https://doi.org/10.1021/jp710675m.

[33] L. Trotochaud, S.L. Young, J.K. Ranney, S.W. Boettcher, Nickel-Iron oxyhydroxide oxygen-evolution electrocatalysts: The role of intentional and incidental iron incorporation, J. Am. Chem. Soc. 136 (2014) 6744–6753. https://doi.org/10.1021/ja502379c.

[34] T. Tian, M. Zheng, J. Lin, X. Meng, Y. Ding, Amorphous Ni-Fe double hydroxide hollow nanocubes enriched with oxygen vacancies as efficient electrocatalytic water oxidation catalysts, Chem. Commun. 55 (2019) 1044–1047. https://doi.org/10.1039/c8cc08511k.

[35] Z. Wang, Q. Lei, Z. Wang, H. Yuan, L. Cao, N. Qin, Z. Lu, J. Xiao, J. Liu, In-situ synthesis of free-standing FeNi-oxyhydroxide nanosheets as a highly efficient electrocatalyst for water oxidation, Chem. Eng. J. 395 (2020) 125180. https://doi.org/10.1016/j.cej.2020.125180.

[36] Y. Liu, Y. Ying, L. Fei, Y. Liu, Q. Hu, G. Zhang, S.Y. Pang, W. Lu, C.L. Mak, X. Luo, L. Zhou, M. Wei, H. Huang, Valence engineering via selective atomic substitution on tetrahedral sites in spinel oxide for highly enhanced oxygen evolution catalysis, J. Am. Chem. Soc. 141 (2020) 8136–8145. https://doi.org/10.1021/jacs.8b13701.

[37] Y. Jin, S. Huang, X. Yue, H. Du, P.K. Shen, Mo- and Fe-Modified $Ni(OH)_2$/NiOOH Nanosheets as Highly Active and Stable Electrocatalysts for Oxygen Evolution Reaction, ACS Catal. 8 (2018) 2359–2363. https://doi.org/10.1021/acscatal.7b04226.

[38] C. Hu, L. Zhang, J. Gong, Recent progress made in the mechanism comprehension and design of electrocatalysts for alkaline water splitting, Energy Environ. Sci. 12 (2019) 2620–2645. https://doi.org/10.1039/c9ee01202h.

[39] L.F. Li, Y.F. Li, Z.P. Liu, Oxygen Evolution Activity on NiOOH Catalysts: Four-

Coordinated Ni Cation as the Active Site and the Hydroperoxide Mechanism, ACS Catal. 10 (2020) 2581–2590. https://doi.org/10.1021/acscatal.9b04975.

[40] Z.W. Gao, J.Y. Liu, X.M. Chen, X.L. Zheng, J. Mao, H. Liu, T. Ma, L. Li, W.C. Wang, X.W. Du, Engineering NiO/NiFe LDH Intersection to Bypass Scaling Relationship for Oxygen Evolution Reaction via Dynamic Tridimensional Adsorption of Intermediates, Adv. Mater. 31 (2019) 1–8. https://doi.org/10.1002/adma.201804769.

[41] B. Weng, F. Xu, C. Wang, W. Meng, C.R. Grice, Y. Yan, A layered $Na_{1-x}Ni_yFe_{1-y}O_2$ double oxide oxygen evolution reaction electrocatalyst for highly efficient water-splitting, Energy Environ. Sci. 10 (2017) 121–128. https://doi.org/10.1039/c6ee03088b.

[42] S. Hao, L. Chen, C. Yu, B. Yang, Z. Li, Y. Hou, L. Lei, X. Zhang, NiCoMo Hydroxide nanosheet arrays synthesized via chloride corrosion for overall water splitting, ACS Energy Lett. 4 (2019) 952–959. https://doi.org/10.1021/acsenergylett.9b00333.

[43] M.A. Sayeed, A.P. O'Mullane, Electrocatalytic water oxidation at amorphous trimetallic oxides based on FeCoNiO:X, RSC Adv. 7 (2017) 43083–43089. https://doi.org/10.1039/c7ra07995h.

[44] V. Maruthapandian, M. Mathankumar, V. Saraswathy, B. Subramanian, S. Muralidharan, Study of the Oxygen Evolution Reaction Catalytic Behavior of $Co_xNi_{1-x}Fe_2O_4$ in Alkaline Medium, ACS Appl. Mater. Interfaces. 9 (2017) 13132–13141. https://doi.org/10.1021/acsami.6b16685.

[45] T. Gao, Z. Jin, M. Liao, J. Xiao, H. Yuan, D. Xiao, A trimetallic V-Co-Fe oxide nanoparticle as an efficient and stable electrocatalyst for oxygen evolution reaction, J. Mater. Chem. A. 3 (2015) 17763–17770. https://doi.org/10.1039/c5ta04058b.

[46] F. Qin, Z. Zhao, M.K. Alam, Y. Ni, F. Robles-Hernandez, L. Yu, S. Chen, Z. Ren, Z. Wang,

J. Bao, Trimetallic NiFeMo for Overall Electrochemical Water Splitting with a Low Cell Voltage, ACS Energy Lett. 3 (2018) 546–554. https://doi.org/10.1021/acsenergylett.7b01335.

[47] H. Gatemala, S. Kosasang, M. Sawangphruk, Bifunctional electrocatalytic CoNi-doped manganese oxide produced from microdumbbell manganese carbonate towards oxygen reduction and oxygen evolution reactions, Sustain. Energy Fuels. 2 (2018) 1170–1177. https://doi.org/10.1039/c8se00062j.

[48] J. Fan, Z. Chen, H. Shi, G. Zhao, In situ grown, self-supported iron-cobalt-nickel alloy amorphous oxide nanosheets with low overpotential toward water oxidation, Chem. Commun. 52 (2016) 4290–4293. https://doi.org/10.1039/c5cc09699e.

[49] J.B. Gerken, S.E. Shaner, R.C. Massé, N.J. Porubsky, S.S. Stahl, A survey of diverse earth abundant oxygen evolution electrocatalysts showing enhanced activity from Ni-Fe oxides containing a third metal, Energy Environ. Sci. 7 (2014) 2376–2382. https://doi.org/10.1039/c4ee00436a.

[50] B. Liu, M. Zhang, Y. Wang, Z. Chen, K. Yan, Facile synthesis of defect-rich ultrathin NiCo-LDHs, NiMn-LDHs and NiCoMn-LDHs nanosheets on Ni foam for enhanced oxygen evolution reaction performance, J. Alloys Compd. 852 (2021) 156949. https://doi.org/10.1016/j.jallcom.2020.156949.

[51] F.-L. Li, Q. Shao, X. Huang, J.-P. Lang, Nanoscale Trimetallic Metal-Organic Frameworks Enable Efficient Oxygen Evolution Electrocatalysis, Angew. Chemie. 130 (2018) 1906–1910. https://doi.org/10.1002/ange.201711376.

[52] F.L. Li, Q. Shao, X. Huang, J.P. Lang, Nanoscale Trimetallic Metal–Organic Frameworks Enable Efficient Oxygen Evolution Electrocatalysis, Angew. Chemie - Int. Ed. 57 (2018)

1888–1892. https://doi.org/10.1002/anie.201711376.

[53] P.-F. Guo, Y. Yang, W.-J. Wang, B. Zhu, W.-T. Wang, Z.-Y. Wang, J.-L. Wang, K. Wang, Z.-H. He, Z.-T. Liu, Stable and active NiFeW layered double hydroxide for enhanced electrocatalytic oxygen evolution reaction, Chem. Eng. J. 426 (2021) 130768. https://doi.org/10.1016/j.cej.2021.130768.

[54] Y. Pi, Q. Shao, P. Wang, F. Lv, S. Guo, J. Guo, X. Huang, Trimetallic Oxyhydroxide Coralloids for Efficient Oxygen Evolution Electrocatalysis, Angew. Chemie - Int. Ed. 56 (2017) 4502–4506. https://doi.org/10.1002/anie.201701533.

[55] Y.T. Lu, Y.J. Chien, C.F. Liu, T.H. You, C.C. Hu, Active site-engineered bifunctional electrocatalysts of ternary spinel oxides, $M_{0.1}Ni_{0.9}Co_2O_4$ (M: Mn, Fe, Cu, Zn) for the air electrode of rechargeable zinc-air batteries, J. Mater. Chem. A. 5 (2017) 21016–21026. https://doi.org/10.1039/c7ta06302d.

[56] P. Sivakumar, P. Subramanian, T. Maiyalagan, A. Gedanken, A. Schechter, Ternary nickel–cobalt–manganese spinel oxide nanoparticles as heterogeneous electrocatalysts for oxygen evolution and oxygen reduction reaction, Mater. Chem. Phys. 229 (2019) 190–196. https://doi.org/10.1016/j.matchemphys.2019.03.017.

[57] X. Jia, S. Gao, T. Liu, D. Li, P. Tang, Y. Feng, Fabrication and Bifunctional Electrocatalytic Performance of Ternary CoNiMn Layered Double Hydroxides/Polypyrrole/Reduced Graphene Oxide Composite for Oxygen Reduction and Evolution Reactions, Electrochim. Acta. 245 (2017) 59–68. https://doi.org/10.1016/j.electacta.2017.05.120.

[58] Y. Yang, L. Dang, M.J. Shearer, H. Sheng, W. Li, J. Chen, P. Xiao, Y. Zhang, R.J. Hamers, S. Jin, Highly Active Trimetallic NiFeCr Layered Double Hydroxide Electrocatalysts for Oxygen Evolution Reaction, Adv. Energy Mater. 8 (2018) 1–9.

https://doi.org/10.1002/aenm.201703189.

[59] S. Hao, G. Zheng, S. Gao, L. Qiu, N. Xu, Y. He, L. Lei, X. Zhang, In Situ Synthesis of Ternary NiCoRu-Based Layered Double Hydroxide by Chlorine Corrosion toward Electrocatalytic Water Oxidation, ACS Sustain. Chem. Eng. 7 (2019) 14361–14367. https://doi.org/10.1021/acssuschemeng.9b03830.

[60] Z. Cai, L. Li, Y. Zhang, Z. Yang, J. Yang, Y. Guo, L. Guo, Amorphous Nanocages of Cu-Ni-Fe Hydr(oxy)oxide Prepared by Photocorrosion For Highly Efficient Oxygen Evolution, Angew. Chemie - Int. Ed. 58 (2019) 4189–4194. https://doi.org/10.1002/anie.201812601.

[61] H.R. Devi, R. Nandan, K.K. Nanda, Mechanistic investigation into efficient water oxidation by Co-Ni based hybrid oxide-hydroxide flowers, ACS Appl. Mater. Interfaces. (2020) acsami.9b22956. https://doi.org/10.1021/acsami.9b22956.

[62] J. Zaffran, M.C. Toroker, Understanding the Oxygen Evolution Reaction on a Two-Dimensional NiO_2 Catalyst, ChemElectroChem. 4 (2017) 2764–2770. https://doi.org/10.1002/celc.201700445.

[63] X. Long, Z. Ma, H. Yu, X. Gao, X. Pan, X. Chen, S. Yang, Z. Yi, Porous FeNi oxide nanosheets as advanced electrochemical catalysts for sustained water oxidation, J. Mater. Chem. A. 4 (2016) 14939–14943. https://doi.org/10.1039/c6ta05907d.

[64] W.J. Jiang, T. Tang, T. Tang, Y. Zhang, J.S. Hu, J.S. Hu, Synergistic Modulation of Non-Precious-Metal Electrocatalysts for Advanced Water Splitting, Acc. Chem. Res. 53 (2020) 1111–1123. https://doi.org/10.1021/acs.accounts.0c00127.

[65] H.R. Devi, R. Nandan, K.K. Nanda, Mechanistic Investigation into Efficient Water Oxidation by Co-Ni-Based Hybrid Oxide-Hydroxide Flowers, ACS Appl. Mater. Interfaces. 12 (2020) 13888–13895. https://doi.org/10.1021/acsami.9b22956.

[66] X. Chen, Capturing the active sites of multimetallic (oxy)hydroxides for the oxygen evolution reaction, Energy Environ. Sci. 13 (2020) 4225–4237. https://doi.org/10.1039/d0ee01609h.

[67] X. Bo, Y. Li, R.K. Hocking, C. Zhao, NiFeCr Hydroxide Holey Nanosheet as Advanced Electrocatalyst for Water Oxidation, ACS Appl. Mater. Interfaces. 9 (2017) 41239–41245. https://doi.org/10.1021/acsami.7b12629.

[68] E. Fabbri, A. Habereder, K. Waltar, R. Kötz, T.J. Schmidt, Developments and perspectives of oxide-based catalysts for the oxygen evolution reaction, Catal. Sci. Technol. 4 (2014) 3800–3821. https://doi.org/10.1039/c4cy00669k.

[69] I.C. Man, H.Y. Su, F. Calle-Vallejo, H.A. Hansen, J.I. Martínez, N.G. Inoglu, J. Kitchin, T.F. Jaramillo, J.K. Nørskov, J. Rossmeisl, Universality in Oxygen Evolution Electrocatalysis on Oxide Surfaces, ChemCatChem. 3 (2011) 1159–1165. https://doi.org/10.1002/cctc.201000397.

[70] J.S. Kim, B. Kim, H. Kim, K. Kang, Recent Progress on Multimetal Oxide Catalysts for the Oxygen Evolution Reaction, Adv. Energy Mater. 8 (2018) 1–26. https://doi.org/10.1002/aenm.201702774.

[71] X-Ray Absorption: Principles, Applications, Techniques of EXAFS, SEXAFS and XANES, edited by D.C. Konigsberger and R. Prince (Wiley, New York, 1988).

[72] X. Zhao, J. Hu, B. Wu, A. Banerjee, S. Chakraborty, J. Feng, Z. Zhao, S. Chen, R. Ahuja, T.C. Sum, Z. Chen, Simultaneous enhancement in charge separation and onset potential for water oxidation in a BiVO4 photoanode by W-Ti codoping, J. Mater. Chem. A. 6 (2018) 16965–16974. https://doi.org/10.1039/c8ta05491f.

[73] G. Natu, P. Hasin, Z. Huang, Z. Ji, M. He, Y. Wu, Valence band-edge engineering of nickel

oxide nanoparticles via cobalt doping for application in p-type dye-sensitized solar cells, ACS Appl. Mater. Interfaces. 4 (2012) 5922–5929. https://doi.org/10.1021/am301565j.

[74] X. Zhao, J. Feng, N. Wang, X. Yao, W. Chen, S. Chen, Z. Huang, Z. Chen, The Influence of Ti Doping on Morphology and Photoelectrochemical Properties of Hematite Grown from Aqueous Solution for Water Splitting, Energy Technol. 6 (2018) 2188–2199. https://doi.org/10.1002/ente.201800286.

[75] D.K. Singh, R.K. Pant, K.K. Nanda, S.B. Krupanidhi, Differentiation of ultraviolet/visible photons from near infrared photons by MoS_2/GaN/Si-based photodetector, Appl. Phys. Lett. 119 (2021). https://doi.org/10.1063/5.0060403.

[76] A.M. Chowdhury, D.K. Singh, B. Roul, K.K. Nanda, S.B. Krupanidhi, Overcoming the Challenges Associated with the InN/InGaN Heterostructure via a Nanostructuring Approach for Broad Band Photodetection, ACS Appl. Electron. Mater. 3 (2021) 4243–4253. https://doi.org/10.1021/acsaelm.1c00695.

[77] B.S. Yeo, A.T. Bell, Enhanced activity of gold-supported cobalt oxide for the electrochemical evolution of oxygen, J. Am. Chem. Soc. 133 (2011) 5587–5593. https://doi.org/10.1021/ja200559j.

[78] J. Zhou, M. Min, Y. Liu, J. Tang, W. Tang, Layered assembly of NiMn-layered double hydroxide on graphene oxide for enhanced non-enzymatic sugars and hydrogen peroxide detection, Sensors Actuators, B Chem. 260 (2018) 408–417. https://doi.org/10.1016/j.snb.2018.01.072.

[79] X. Hu, H. Huang, J. Zhang, J. Shi, S. Zhu, N. Su, Controllable hydrothermal-assisted synthesis of mesoporous Co_3O_4 nanosheets, RSC Adv. 5 (2015) 99899–99906. https://doi.org/10.1039/c5ra19789a.

[80] M.H. Mamat, N. Parimon, A.S. Ismail, I.B. Shameem Banu, S. Sathik Basha, G. V. Vijayaraghavan, M.K. Yaakob, A.B. Suriani, M.K. Ahmad, M. Rusop, Structural, optical, and electrical evolution of sol–gel-immersion grown nickel oxide nanosheet array films on aluminium doping, J. Mater. Sci. Mater. Electron. 30 (2019) 9916–9930. https://doi.org/10.1007/s10854-019-01330-z.

[81] Z. Huang, W. Zhou, C. Ouyang, J. Wu, F. Zhang, J. Huang, Y. Gao, J. Chu, High performance of Mn-Co-Ni-O spinel nanofilms sputtered from acetate precursors, Sci. Rep. 5 (2015) 2–9. https://doi.org/10.1038/srep10899.

[82] X. Feng, C. Chen, C. He, S. Chai, Y. Yu, J. Cheng, Non-thermal plasma coupled with MOF-74 derived Mn-Co-Ni-O porous composite oxide for toluene efficient degradation, J. Hazard. Mater. 383 (2020) 121143. https://doi.org/10.1016/j.jhazmat.2019.121143.

[83] T. Takahagi, a. Ishitani, Xps Study on the Surface Structure of, Carbon N. Y. 26 (1988) 389–396. https://doi.org/10.1016/0008-6223(88)90231-X.

[84] R. Wu, D.P. Wang, K. Zhou, N. Srikanth, J. Wei, Z. Chen, Porous cobalt phosphide/graphitic carbon polyhedral hybrid composites for efficient oxygen evolution reactions, J. Mater. Chem. A. 4 (2016) 13742–13745. https://doi.org/10.1039/c6ta05679b.

[85] S. V. Devaguptapu, S. Hwang, S. Karakalos, S. Zhao, S. Gupta, D. Su, H. Xu, G. Wu, Morphology Control of Carbon-Free Spinel $NiCo_2O_4$ Catalysts for Enhanced Bifunctional Oxygen Reduction and Evolution in Alkaline Media, ACS Appl. Mater. Interfaces. 9 (2017) 44567–44578. https://doi.org/10.1021/acsami.7b16389.

[86] J. Jiang, F. Sun, S. Zhou, W. Hu, H. Zhang, J. Dong, Z. Jiang, J. Zhao, J. Li, W. Yan, M. Wang, Atomic-level insight into super-efficient electrocatalytic oxygen evolution on iron and vanadium co-doped nickel (oxy)hydroxide, Nat. Commun. 9 (2018) 1–12.

https://doi.org/10.1038/s41467-018-05341-y.

[87] R.D.L. Smith, M.S. Prévot, R.D. Fagan, S. Trudel, C.P. Berlinguette, Water oxidation catalysis: Electrocatalytic response to metal stoichiometry in amorphous metal oxide films containing iron, cobalt, and nickel, J. Am. Chem. Soc. 135 (2013) 11580–11586. https://doi.org/10.1021/ja403102j.

[88] N. Weidler, J. Schuch, F. Knaus, P. Stenner, S. Hoch, A. Maljusch, R. Schäfer, B. Kaiser, W. Jaegermann, X-ray Photoelectron Spectroscopic Investigation of Plasma-Enhanced Chemical Vapor Deposited NiOx, NiOx(OH)y, and CoNiOx(OH)y: Influence of the Chemical Composition on the Catalytic Activity for the Oxygen Evolution Reaction, J. Phys. Chem. C. 121 (2017) 6455–6463. https://doi.org/10.1021/acs.jpcc.6b12652.

[89] S. Hao, L. Chen, C. Yu, B. Yang, Z. Li, Y. Hou, L. Lei, X. Zhang, NiCoMo Hydroxide nanosheet arrays synthesized via chloride corrosion for overall water splitting, ACS Energy Lett. 4 (2019) 952–959. https://doi.org/10.1021/acsenergylett.9b00333.

[90] T. Tang, W.J. Jiang, S. Niu, N. Liu, H. Luo, Y.Y. Chen, S.F. Jin, F. Gao, L.J. Wan, J.S. Hu, Electronic and Morphological Dual Modulation of Cobalt Carbonate Hydroxides by Mn Doping toward Highly Efficient and Stable Bifunctional Electrocatalysts for Overall Water Splitting, J. Am. Chem. Soc. 139 (2017) 8320–8328. https://doi.org/10.1021/jacs.7b03507.

[91] Q. Zhao, J. Yang, M. Liu, R. Wang, G. Zhang, H. Wang, H. Tang, C. Liu, Z. Mei, H. Chen, F. Pan, Tuning Electronic Push/Pull of Ni-Based Hydroxides to Enhance Hydrogen and Oxygen Evolution Reactions for Water Splitting, ACS Catal. 8 (2018) 5621–5629. https://doi.org/10.1021/acscatal.8b01567.

[92] T. Tian, H. Gao, X. Zhou, L. Zheng, J. Wu, K. Li, Y. Ding, Study of the Active Sites in Porous Nickel Oxide Nanosheets by Manganese Modulation for Enhanced Oxygen

Evolution Catalysis, ACS Energy Lett. 3 (2018) 2150–2158. https://doi.org/10.1021/acsenergylett.8b01206.

[93] O.Y. Bisen, A.K. Yadav, K.K. Nanda, Self-Organized Single-Atom Tungsten Supported on the N-Doped Carbon Matrix for Durable Oxygen Reduction, ACS Appl. Mater. Interfaces. 12 (2020) 43586–43595. https://doi.org/10.1021/acsami.0c10234.

[94] W. Li, D. Xiong, X. Gao, L. Liu, The oxygen evolution reaction enabled by transition metal phosphide and chalcogenide pre-catalysts with dynamic changes, Chem. Commun. 55 (2019) 8744–8763. https://doi.org/10.1039/c9cc02845e.

[95] X. Cao, Y. Hong, N. Zhang, Q. Chen, J. Masud, M.A. Zaeem, M. Nath, Phase Exploration and Identification of Multinary Transition-Metal Selenides as High-Efficiency Oxygen Evolution Electrocatalysts through Combinatorial Electrodeposition, ACS Catal. 8 (2018) 8273–8289. https://doi.org/10.1021/acscatal.8b01977.

[96] A.T. Swesi, J. Masud, M. Nath, Nickel selenide as a high-efficiency catalyst for oxygen evolution reaction, Energy Environ. Sci. 9 (2016) 1771–1782. https://doi.org/10.1039/c5ee02463c.

[97] E.S. Material, T.R. Society, Electronic Supplementary information Synergism between polydopamine and polyurethane in the synthesis of Ni-Fe alloy monoliths, (2014).

[98] H.R. Devi, B.C. Ong, X. Zhao, Z. Dong, K.K. Nanda, Z. Chen, Insights into Improving Photoelectrochemical Water-Splitting Performance Using Hematite Anode, Energy Technol. 2100457 (2021). https://doi.org/10.1002/ente.202100457.

[99] T.E. Kibona, Synthesis of $NiCo_2O_4$ / mesoporous carbon composites for supercapacitor electrodes, (2020) 1587–1598.

[100] G.-B. Wang, C.-S. Hsu, H.M. Chen, Individual role of active sites in bimetallic oxygen

evolution reaction catalysts, Dalt. Trans. (2020). https://doi.org/10.1039/d0dt03448g.

[101] R. Nandan, S. Nanda, Cyanogenic glycosides: A sustainable carbon and nitrogen source for developing resilient Janus reversible oxygen electrocatalysts for metal-air batteries, Carbon N. Y. 155 (2019) 155–165. https://doi.org/10.1016/j.carbon.2019.08.053.

[102] R. Nandan, H.R. Devi, R. Kumar, A.K. Singh, C. Srivastava, K.K. Nanda, Inner Sphere Electron Transfer Promotion on Homogeneously Dispersed Fe-Nx Centers for Energy-Efficient Oxygen Reduction Reaction, ACS Appl. Mater. Interfaces. 12 (2020) 36026–36039. https://doi.org/10.1021/acsami.0c08086.

[103] E. Miralles, R. Compañó, M. Granados, M.D. Prat, Determination of metal-cyanide complexes by ion-interaction chromatography with fluorimetric detection, Anal. Chim. Acta. 403 (2000) 197–204. https://doi.org/10.1016/S0003-2670(99)00603-0.

[104] S.R. Wild, T. Rudd, A. Neller, Fate and effects of cyanide during wastewater treatment processes, Sci. Total Environ. 156 (1994) 93–107. https://doi.org/10.1016/0048-9697(94)90346-8.

[105] R. Nandan, A. Gautam, K.K. Nanda, Anthocephalus cadamba shaped FeNi encapsulated carbon nanostructures for metal-air batteries as a resilient bifunctional oxygen electrocatalyst, J. Mater. Chem. A. 6 (2018) 20411–20420. https://doi.org/10.1039/c8ta05822a.

[106] B.K. Barman, D. Das, K.K. Nanda, Sustainable Energy & Fuels Facile synthesis of ultra fi ne Ru nanocrystal supported N-doped graphene as an exceptional hydrogen evolution electrocatalyst in both alkaline and acidic media †, Sustain. Energy Fuels. 1 (2017) 1028–1033. https://doi.org/10.1039/c7se00153c.

[107] R. Nandan, A. Gautam, S. Tripathi, K.K. Nanda, A comprehensive analysis and rational

designing of efficient Fe-based oxygen electrocatalysts for metal-air batteries, J. Mater. Chem. A. 6 (2018) 8537–8548. https://doi.org/10.1039/c8ta01938j.

[108] X. Du, H. Su, X. Zhang, Metal-Organic Framework-Derived Cu-Doped Co9S8 Nanorod Array with Less Low-Valence Co Sites as Highly Efficient Bifunctional Electrodes for Overall Water Splitting, ACS Sustain. Chem. Eng. 7 (2019) 16917–16926. https://doi.org/10.1021/acssuschemeng.9b04739.

[109] A. Adán-Más, T.M. Silva, L. Guerlou-Demourgues, M.F. Montemor, Application of the Mott-Schottky model to select potentials for EIS studies on electrodes for electrochemical charge storage, Electrochim. Acta. 289 (2018) 47–55. https://doi.org/10.1016/j.electacta.2018.08.077.

[110] Krishnan Rajeshwar, Fundamentals of Semiconductor Electrochemistry and Photoelectrochemistry, Encycl. Electrochem. (2002). https://doi.org/10.1002/9783527610426.bard060001.

[111] X.G. Zhang, Electrochemistry of Silicon and its oxide, Kluwer Academic, 1387.

[112] S.A. Bonke, A.M. Bond, L. Spiccia, A.N. Simonov, Parameterization of Water Electrooxidation Catalyzed by Metal Oxides Using Fourier Transformed Alternating Current Voltammetry, J. Am. Chem. Soc. 138 (2016) 16095–16104. https://doi.org/10.1021/jacs.6b10304.

[113] J. Song, C. Wei, Z.F. Huang, C. Liu, L. Zeng, X. Wang, Z.J. Xu, A review on fundamentals for designing oxygen evolution electrocatalysts, Chem. Soc. Rev. 49 (2020) 2196–2214. https://doi.org/10.1039/c9cs00607a.

[114] J. Zhang, H.B. Tao, M. Kuang, H. Bin Yang, W. Cai, Q. Yan, Q. Mao, B. Liu, Advances in Thermodynamic-Kinetic Model for Analyzing the Oxygen Evolution Reaction, ACS Catal.

10 (2020) 8597–8610. https://doi.org/10.1021/acscatal.0c01906.

[115] X. Bo, R.K. Hocking, S. Zhou, Y. Li, X. Chen, J. Zhuang, Y. Du, C. Zhao, Capturing the active sites of multimetallic (oxy)hydroxides for the oxygen evolution reaction, Energy Environ. Sci. 13 (2020) 4225–4237. https://doi.org/10.1039/d0ee01609h.

[116] P.F. Liu, S. Yang, L.R. Zheng, B. Zhang, H.G. Yang, Mo^{6+} activated multimetal oxygen-evolving catalysts, Chem. Sci. 8 (2017) 3484–3488. https://doi.org/10.1039/c6sc04819f.

[117] B. Zhang, X. Zheng, O. Voznyy, R. Comin, M. Bajdich, M. García-Melchor, L. Han, J. Xu, M. Liu, L. Zheng, F.P.G. De Arquer, C.T. Dinh, F. Fan, M. Yuan, E. Yassitepe, N. Chen, T. Regier, P. Liu, Y. Li, P. De Luna, A. Janmohamed, H.L. Xin, H. Yang, A. Vojvodic, E.H. Sargent, Homogeneously dispersed multimetal oxygen-evolving catalysts, Science (80-.). 352 (2016) 333–337. https://doi.org/10.1126/science.aaf1525.

[118] J. Jiang, F. Sun, S. Zhou, W. Hu, H. Zhang, J. Dong, Z. Jiang, J. Zhao, J. Li, W. Yan, M. Wang, Atomic-level insight into super-efficient electrocatalytic oxygen evolution on iron and vanadium co-doped nickel (oxy)hydroxide, Nat. Commun. 9 (2018) 1–12. https://doi.org/10.1038/s41467-018-05341-y.

[119] X. Chen, Environmental Science (oxy) hydroxides for the oxygen evolution reaction †, (2020) 4225–4237. https://doi.org/10.1039/d0ee01609h.

[120] D. Wu, Y. Wei, X. Ren, X. Ji, Y. Liu, X. Guo, Z. Liu, A.M. Asiri, Q. Wei, X. Sun, $Co(OH)_2$ Nanoparticle-Encapsulating Conductive Nanowires Array: Room-Temperature Electrochemical Preparation for High-Performance Water Oxidation Electrocatalysis, Adv. Mater. 30 (2018) 1–7. https://doi.org/10.1002/adma.201705366.

[121] M. Zhou, Q. Weng, X. Zhang, X. Wang, Y. Xue, X. Zeng, Y. Bando, D. Golberg, In situ electrochemical formation of core-shell nickel-iron disulfide and oxyhydroxide

heterostructured catalysts for a stable oxygen evolution reaction and the associated mechanisms, J. Mater. Chem. A. 5 (2017) 4335–4342. https://doi.org/10.1039/c6ta09366c.

[122] H.S. Sonwalkar, S.K. Haram, Kinetic Analysis of the Oxygen Evolution Reaction (OER) Performed with a Cobalt-Phosphate Electrocatalyst, ChemistrySelect. 2 (2017) 3323–3328. https://doi.org/10.1002/slct.201700282.

[123] R. Guidelli, R.G. Compton, J.M. Feliu, E. Gileadi, J. Lipkowski, W. Schmickler, S. Trasatti, Definition of the transfer coefficient in electrochemistry (IUPAC Recommendations 2014), Pure Appl. Chem. 86 (2014) 259–262. https://doi.org/10.1515/pac-2014-5025.

[124] T. Kessler, W.E. Triaca, A.J. Arvia, Kinetics and mechanism of the oxygen evolution reaction at oxide-coated Co-Ni amorphous alloy electrodes, J. Appl. Electrochem. 24 (1994) 310–315. https://doi.org/10.1007/BF00242058.

TOC

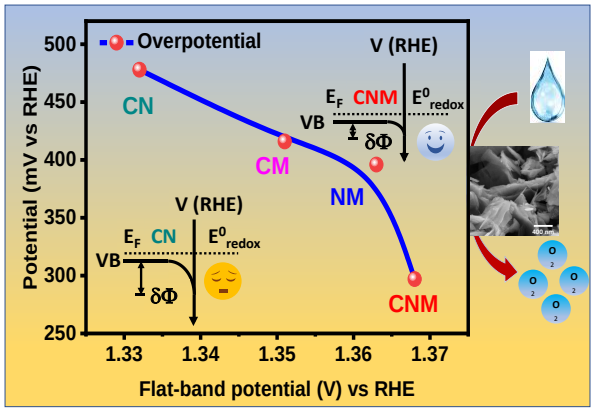

Declaration of interests

☑ The authors declare that they have no known competing financial interests or personal relationships that could have appeared to influence the work reported in this paper.

☐The authors declare the following financial interests/personal relationships which may be considered as potential competing interests: